



AFRL-AFOSR-UK-TR-2019-0007

---

## Hypersonic Transition Experiments in Ludwieg Tubes

Rolf Radespiel  
TECHNISCHE UNIVERSITÄT CAROLO-WILHELMINA ZU BRAUNSCHWEIG  
BIENRODER WEG 3  
BRUNSCHWEIG, 38106  
DE

---

01/29/2019  
Final Report

DISTRIBUTION A: Distribution approved for public release.

Air Force Research Laboratory  
Air Force Office of Scientific Research  
European Office of Aerospace Research and Development  
Unit 4515 Box 14, APO AE 09421

<b>REPORT DOCUMENTATION PAGE</b>					Form Approved OMB No. 0704-0188	
<p>The public reporting burden for this collection of information is estimated to average 1 hour per response, including the time for reviewing instructions, searching existing data sources, gathering and maintaining the data needed, and completing and reviewing the collection of information. Send comments regarding this burden estimate or any other aspect of this collection of information, including suggestions for reducing the burden, to Department of Defense, Executive Services, Directorate (0704-0188). Respondents should be aware that notwithstanding any other provision of law, no person shall be subject to any penalty for failing to comply with a collection of information if it does not display a currently valid OMB control number.</p> <p>PLEASE DO NOT RETURN YOUR FORM TO THE ABOVE ORGANIZATION.</p>						
1. REPORT DATE (DD-MM-YYYY) 29-01-2019		2. REPORT TYPE Final		3. DATES COVERED (From - To) 15 May 2016 to 14 Aug 2018		
4. TITLE AND SUBTITLE Hypersonic Transition Experiments in Ludwig Tubes				5a. CONTRACT NUMBER		
				5b. GRANT NUMBER FA9550-16-1-0285		
				5c. PROGRAM ELEMENT NUMBER 61102F		
6. AUTHOR(S) Rolf Radespiel				5d. PROJECT NUMBER		
				5e. TASK NUMBER		
				5f. WORK UNIT NUMBER		
7. PERFORMING ORGANIZATION NAME(S) AND ADDRESS(ES) TECHNISCHE UNIVERSITÄT CAROLO-WILHELMINA ZU BRAUNSCHWEIG BIENRODER WEG 3 BRUNSCHWEIG, 38106 DE				8. PERFORMING ORGANIZATION REPORT NUMBER		
9. SPONSORING/MONITORING AGENCY NAME(S) AND ADDRESS(ES) EOARD Unit 4515 APO AE 09421-4515				10. SPONSOR/MONITOR'S ACRONYM(S) AFRL/AFOSR IOE		
				11. SPONSOR/MONITOR'S REPORT NUMBER(S) AFRL-AFOSR-UK-TR-2019-0007		
12. DISTRIBUTION/AVAILABILITY STATEMENT A DISTRIBUTION UNLIMITED; PB Public Release						
13. SUPPLEMENTARY NOTES						
14. ABSTRACT <p>The project has accomplished a thorough analysis of measurements taken in two hypersonic Ludwig tubes HLB in Braunschweig and HHK-6 at USAFA in Colorado. The analyses include modal decomposition of tunnel freestream measurements with pitot probes and hot wires, as well as assessment of boundary layer transition measurements on a 7 deg cone and on a blunt capsule model. The results indicate that there exist significantly different freestream disturbance levels in both facilities, particularly for elevated freestream temperatures. The elevated freestream disturbances in HHK-6 affect transition on slender models to a significant extent, as initial amplitudes of the hypersonic second instability modes are larger and break down to turbulence happens earlier. Much lesser differences between both tunnels were observed for boundary layer transition on blunted models with roughness-induced transition.</p>						
15. SUBJECT TERMS hypersonic transition						
16. SECURITY CLASSIFICATION OF:			17. LIMITATION OF ABSTRACT	18. NUMBER OF PAGES	19a. NAME OF RESPONSIBLE PERSON	
a. REPORT	b. ABSTRACT	c. THIS PAGE			SMITH, DOUGLAS	
Unclassified	Unclassified	Unclassified	SAR		19b. TELEPHONE NUMBER (Include area code) 314-235-6013	

**Final Report**  
**Grant No. FA9550-10-1-0285**

# **Hypersonic Transition Experiments in Ludwig Tubes**

Federico Muñoz  
Prof. Dr.-Ing. R. Radespiel  
10 December, 2018

Technische Universität Braunschweig  
Institut für Strömungsmechanik  
**Report Period:** 15 Mai 2016 to 15 August 2018

# Summary

The present research project aimed at measuring the growth of boundary layer instabilities and their response on freestream disturbances for two fundamentally different configurations, blunt and slender bodies. These two configurations are representative for a wide range of hypersonic vehicles. The work is divided into three research lines; the characterization of freestream disturbances in the conventional Ludwieg tubes, transition experiments on cones and transition experiments on blunt models.

Measurements were conducted in the two hypersonic Ludwieg tubes, with a nominal Mach number of 6; one at the US Air Force Academy (USAFA) in Colorado Springs and one at the Technische Universität Braunschweig in Germany. Cone measurements at zero angle of attack showed a second-mode instability dominated transition. The effect of the noise level and stagnation temperatures on the second mode instability were investigated in detail using pressure transducers. The transition onset was studied by means of infrared thermography. Freestream measurements were conducted in both tunnels by means of suited Pitot probes and CTA anemometer. The same sensors and measurement equipment were used in both tunnels. The data obtained from these measurements were analyzed and compared showing higher noise levels at the USAFA wind tunnel. Different approaches to modal decomposition were investigated, and the methodology was compared to results from DNS simulations. From the analyses of modal decomposition of freestream disturbances, the project has derived recommendations of future research in this area, namely to involve further measurement techniques and formal uncertainty quantification techniques.

An instrumented 7-deg cone model served for measuring second-mode instabilities. Amplitudes of instabilities were measured in both facilities along with transition onset. The results showed a significant effect of free-stream disturbances on transition dominated by second modes. An Apollo shape capsule was used to investigate transition on blunt bodies. Transition investigations were conducted using thermocouples. A distributed roughness patch was applied along the symmetry plane of the model. The capsule showed little dependency of the free stream noise with respect to the transition location. The transition locations obtained from the rough surface agree well with the correlation model for transient growth. The results of this investigation can be found in form of several scientific articles.

# Table of contents

<i>Summary</i> .....	<i>I</i>
<i>Table of contents</i> .....	<i>II</i>
<i>List of Figures</i> .....	<i>III</i>
<i>List of abbreviations</i> .....	<i>V</i>
<b>1 Introduction</b> .....	<b>6</b>
<b>1.1 Motivation</b> .....	<b>6</b>
<b>2 Methods, Assumptions and Procedures</b> .....	<b>7</b>
<b>2.1 Experimental Setup</b> .....	<b>7</b>
<b>2.2 Freestream Characterization</b> .....	<b>8</b>
<b>2.3 Slender Body Experiments</b> .....	<b>11</b>
<b>2.4 Blunt Body Experiments</b> .....	<b>13</b>
<b>3 Results and Discussion</b> .....	<b>15</b>
<b>3.1 Freestream Characterization</b> .....	<b>15</b>
<b>A. Hotwire Calibration</b> .....	<b>20</b>
<b>B. Results of Hotwire Measurements</b> .....	<b>21</b>
<b>C. Reconstruction of Freestream Disturbances and Modal Decomposition</b> .....	<b>23</b>
<b>3.2 Cone Measurements</b> .....	<b>26</b>
<b>3.3 Capsule Measurements</b> .....	<b>31</b>
<b>4 Conclusions</b> .....	<b>35</b>
<b>5 References</b> .....	<b>36</b>
<b>6 List of Publications</b> .....	<b>37</b>
<b>7 List of supported personnel</b> .....	<b>38</b>

# List of Figures

Figure 1. Schematic of the hypersonic wind tunnel .....	7
Figure 2. Freestream measurements locations in the test section of the wind tunnels.....	8
Figure 3. Freestream characterization, probe holder for vertical position variation .....	10
Figure 4. Explosion view of the cone model.....	12
Figure 5. Section of the cone model with a description of sensors position .....	12
Figure 6. Sketches of the Apollo shaped capsule model mounted in the wind tunnel with 24° AoA.....	13
Figure 7. Analysis of the stochastic distributed roughness element by means of a laser scan microscope .....	14
Figure 8. Normalized values of RMS pressure fluctuations filtered between 5 kHz and 100 kHz.....	16
Figure 9. Pressure fluctuation for different axial positions in HHK-6 at $T_0=450K$ from PCB sensor, filtered between 5kHz to 100kHz.....	17
Figure 10. Variation of the stagnation pressure along the test section of HHK-6 for $T_0=450K$ .....	17
Figure 11. PSD of pressure fluctuation obtained from PCB and Kulite sensors .....	18
Figure 12. Time traces of hotwire measurements in HLB and HHK-6 at the reference position and $Re/m=10 \cdot 10^6$ .....	19
Figure 13. PSD of the output voltage of the 5 $\mu m$ hotwire, in HLB at $T_0=470$ and HHK-6 at $T_0=450$ and same wire temperatures, normalized by the mean voltage .....	19
Figure 14. Square wave test of the 5 $\mu m$ and 10 $\mu m$ wires signal in HLB at $Re/m=10 \cdot 10^6$ .....	20
Figure 15. PSD of the output voltage between the 5 $\mu m$ and 10 $\mu m$ hotwires in the HLB at $Re/m=10 \cdot 10^6$ .....	20
Figure 16. Determination of the best coefficient for the linear fitting of $E_2 \sim \rho u_n$ .....	20
Figure 17. Mass flow and total temperature fluctuations in HLB and HHK-6 from filtered signals between 5 and 100kHz with the 5 $\mu m$ wire.....	21
Figure 18. Effect of wire on mass flow and total temperature fluctuations in HLB at $T_0=470K$ , $x=300mm$ and $z=100mm$ .....	22
Figure 19. Effect of wire on mass flow and total temperature fluctuations in HLB at $T_0=470K$ , $x=300mm$ and $z=100mm$ .....	22
Figure 20. Comparison of mass flow and total temperature fluctuations between DNS simulation and experimental data in HLB at $T_0=470K$ at $x=300mm$ and $z=100mm$ .....	23
Figure 21. Filtered DNS simulation at the outflow plane of the nozzle compared to filtered data from the measurements in HLB.....	23
Figure 22. Mass flow, total temperature, and pressure fluctuations of DNS and filtered experimental data for $T_0=470K$ at $x=300mm$ and $z=100mm$ .....	24

Figure 23. Mass flow, total temperature, and pressure fluctuations of filtered DNS and experimental data for $T_0=470K$ at $x=300$ and $z=100mm$ .....	24
Figure 24. Freestream temperature, velocity, density and pressure fluctuations computed following Logan's approach compared to DNS data .....	25
Figure 25. Modal decomposition of freestream disturbances in HLB for Logan and Morkovin approaches .....	25
Figure 26. Power density spectra of pressure fluctuations on the surface of the 7deg half angle for two locations in the HHK-6 at $Re/m=8.56e6$ .....	26
Figure 27. Sketch of sensors location distributed in azimuthal direction at the same axial location .....	27
Figure 28. Power density spectra analysis of pressure fluctuations of three sensors distributed in azimuthal direction at the same axial position in HHK-6 at $z=75mm$ .....	28
Figure 29. Noise effect on the second mode instability investigated by changing the vertical position in HHK-6 at different Reynolds numbers.....	29
Figure 30. Temperature effect on the second mode instability investigated by changing the stagnation temperature in HHK-6 at different Reynolds numbers .....	29
Figure 31. RMS values of second mode instabilities in HLB and HHK-6 .....	30
Figure 32. Transition location analysis based on centerline heat flux from infrared thermography.....	31
Figure 33. Heat flux on the capsule surface with variation of $Re/m$ and capsule position in both facilities .....	32
Figure 34. Heat flux on the capsule surface with variation of $Re/m$ and capsule position in both facilities .....	33
Figure 35. Normalized heat flux on the capsule surface with variation of $T_0$ and position in HHK-6 at $Re/m=8.25 \cdot 10^6$ .....	34
Figure 36. Extraction of transition location from heat flux values obtained from the capsule surface at reference position at two conditions showing a) later start of transition onset, b) early transition onset including turbulent flow .....	34
Figure 37. Comparison of transition location on different facilities based on the transient growth theory.....	35

# List of abbreviations

AoA	Angle of Attack
CTA	Constant Temperature Anemometer
DNS	Direct Numerical Simulation
HLB	Hypersonic Ludwig Tube Braunschweig
SPP	Stagnation Point Probe
USAFA	Unite State Air Force Academy



# 1 Introduction

## 1.1 Motivation

The design of high-speed vehicles is directly related to an accurate prediction of aerodynamic and thermal loads. These loads are governed by the boundary layer. The higher shear stresses present in turbulent boundary layers result in higher heat flux values than in laminar ones. Although it is possible to accurately determine the thermal loads in both cases, the location where this transition from laminar to turbulent boundary layer occurs is difficult to predict, and a major challenge for hypersonic simulations.

The transition process is associated with the growth and final breakdown of instabilities inside the laminar boundary layer. Despite of long-lasting efforts, the physical effects leading to transition are not understood for many cases, because of the, in comparison to subsonic flow, higher complexity and amount of variables involved in experimental validation of analytical theories. To better understand the physical mechanisms involved in the transition process, experimental investigations in ground facilities are necessary where the influence of different parameters such as geometry, Reynolds number, total temperature, wall temperature, etc. can be analyzed in detail. In contrast to flight test, the freestream entering the test section of the high speed wind tunnel is highly unsteady. The unsteadiness is caused by the fluctuations of usually all flow variables. This project aimed at measuring the development of boundary layer instabilities and their response to freestream disturbances for slender and blunt bodies. These two configurations are representative for a wide range of hypersonic vehicles. A 7 deg sharp half-angle cone was used to conduct experiments on slender bodies and an Apollo shape capsule was employed to investigate the flow around blunt bodies.

Measurements were performed in two hypersonic facilities of the Ludwieg tube type, located at Technische Universität Braunschweig in Germany and at US Air Force Academy in Colorado Springs. The facilities have the same nozzle and test section geometries, but they exhibit different storage tubes, which results in different freestream disturbance spectra. Thus, the project was divided into parts, firstly the thorough characterization of the freestream disturbances by means of stagnation point probes and hotwire, and secondly the investigation of the boundary layer instabilities and transition process using infrared thermography, pressure sensors, and thermocouples.

In axisymmetric hypersonic cone flows the two most amplified instabilities are the Tollmien-Schlichting (TS) and the second-mode instability [1]. The latter one dominates transition for boundary layer edge Mach numbers above 4. Second-mode instabilities are trapped acoustic waves that bounce between the wall and the sonic line inside the boundary layer, traveling with 90% of the boundary layer edge velocity. Although linear stability theory has shown to be a valuable tool for predicting transition of second-mode instabilities, a large discrepancy in the transition Reynolds numbers is found when measurements are conducted in different facilities [2]. This variation of the transition Reynolds number is mainly caused by the difference in the noise levels. Pate collected experimental results from different supersonic and hypersonic wind tunnels with Mach numbers between 3 to 20 for conical flows and developed a correlation method, which shows that the transition Reynolds number of the second mode can be correlated to the noise level and size of the facility [3]. Hence, the technical problem, in this case, is to understand the receptivity process, which is responsible for the initial amplitudes of the modal instability and how this influences the transition process. Differently, stagnation flows are subject to other types of growing disturbances in the boundary layer. The compressible

boundary layer that forms on spheres does not show harmonic mode instabilities, up to very high Reynolds numbers. Typically, distributed roughness on the surface, combined with an accelerated flow, generates small vortices inside the boundary layer that grow and cause break down to turbulence. The principal mechanism that causes these instabilities to grow is the transient growth, according to Reshotko and Tumin [4].

During the first year of the project, freestream measurements were conducted in both facilities. A novel modal decomposition method was then developed considering information gained from DNS simulations of the stagnation point probes. Moreover, second mode instabilities and transition Reynolds numbers were measured on the cone model. During the second year, measurements were conducted on a blunt body in both facilities with and without stochastically distributed roughness elements. Also additional measurements using different hot wires were performed in HLB to validate previous ones. To reduce the uncertainties and improve comparability of the results, the same equipment and sensors used to carry out all measurements in both facilities. The validity of the hot wire decomposition method and its assumptions were scrutinized comparing the results to newly available data from DNS simulations of the wind tunnel nozzle.

## **2 Methods, Assumptions and Procedures**

### **2.1 Experimental Setup**

The measurements were performed in the Hypersonic Ludwig Tube Braunschweig (HLB) at the TU Braunschweig in Germany, and in the HHK-6 at the USAF Academy in Colorado Springs, USA. A schematic of the facilities is shown in Figure 1. The wind tunnel is composed of a storage tube, which functions as a pressure reservoir and contains the air used during the measurements, a fast-acting valve that separates the high pressure from the low pressure sections, a Laval nozzle that expands the flow into the test section at Mach 6, a test section 0.5m in diameter, and a large vacuum tank, which is designed to maintain low pressures during and after the run. The nozzle has a terminating opening angle of  $3^\circ$  at the test section interface, which results in a slight flow expansion along the test section. The wind tunnel starts when the fast acting valve is opened, connecting the high pressure with the low-pressure parts of the tunnel. At this moment, an expansion wave travels through the storage tube and is later reflected at the end of the storage tube. Before the reflected wave returns, the valve is closed. During this time, nearly constant flow conditions are established in the test section.

**Figure 1. Schematic of the hypersonic wind tunnel**

Although both facilities have the same nozzle and same working principle, differences exist between the facilities that must be addressed. The HLB storage tube is 17m long, while the USAFA HHK-6 is 27m long. The HHK-6 storage tube is heated over its entire length, while the HLB is only heated for the last 3m upstream of the nozzle. Also, the available range of total temperatures and Reynolds numbers are different for both facilities. The following table quantifies the differences between the two facilities.

**Table 1. HLB and USAFA HHK-6 operating conditions**

	<b>TU Braunschweig, HLB</b>	<b>USAFA, HHK-6</b>
Mach number	5.85-5.95	5.85-5.95
Storage Tube pressure	4-30 bar	4-40 bar
Reynolds numbers	$Re/m = 2.5-22 \cdot 10^6$	$Re/m = 1.9-30 \cdot 10^6$
Total Temperature	up to 470 K	up to 670 K
Storage Tube length	17m (3m heated)	27m (completely heated)
Nominal running time	~80 ms	~120 ms

## 2.2 Freestream Characterization

### A. Pitot Pressure Measurements

Freestream measurements were conducted in both wind tunnels under similar flow conditions. These measurements were performed more in detail in the HHK-6 including more measurement points and flow conditions. A schematic representation of the measured points in the test section is presented in Figure 2. Pitot and hotwire measurements were performed at  $x=300\text{mm}$  and  $x=0\text{mm}$  (nozzle outflow plane). At  $x=300\text{mm}$  the probe was moved vertically in 25mm steps from the center axis ( $z=0\text{mm}$ ) to  $z=100\text{mm}$ . Furthermore, measurements were conducted at  $x=0$  at two different heights  $z=0\text{mm}$  and  $z=100\text{mm}$ .

**Figure 2. Freestream measurements locations in the test section of the wind tunnels**

The pressure measurements were conducted by means of a pitot probe. In order to capture the pressure fluctuations for a broad frequency range the measurements were performed with two transducers; one Kulite sensor of type XCS-062-50PSIA (B screen) which is capable of measuring absolute pressures, and a PCB sensor of type 132B38 which only measures pressures fluctuations. In this way, it is possible to validate the obtained data by using two different instruments and extend the frequency resolution. While the Kulite sensors could resolve from 0 Hz up to 30kHz, the PCB sensor provides useful values of pressure fluctuations from 7kHz

to 1MHz. Using the two sensors, it is possible to obtain the mean pressures and better accuracy in the pressure fluctuations.

The sensors were flush mounted on a single element support shown in Figure 3. The shape of the holder has an important effect on the pressure fluctuations which are measured. Numerical simulations and experimental data showed that a probe with round edges is more suitable for freestream pressure measurements than using a cylindrical probe or a probe with 45° chamfering at the corner [5]. The probe consists of a wedge holding an 8 mm diameter tube with interchangeable tips. One tip was constructed for carrying the PCB sensor with a diameter of 3.18 mm, and another to hold the Kulite sensor with a diameter of 1.7 mm.

The pitot probe yields the stagnation pressure behind the detached shock, but the static pressure fluctuation is also needed. Hence, a transfer function of the stagnation pressure fluctuation behind the shock to the static pressure fluctuation ahead of the shock is necessary. Furthermore, the stagnation pressure fluctuations include both: stagnation pressure fluctuations generated by freestream acoustic and entropy disturbances after crossing the shock wave ahead of the probe tip. Recent DNS calculations of the probe used allows applying a transfer function to reconstruct original pressure fluctuations [6].

## B. Hotwire

The freestream is characterized by decomposing the disturbances into fluctuations of flow variables ( $\rho$ ,  $u$ ,  $p$  and  $T$ ). A Constant Temperature Anemometer (CTA) system allows measuring mass flow and total temperature fluctuations from which further flow variables can be computed. The system used consists of a DANTEC Stream Line Pro frame with a CTA bridge with a 1:20 ratio (the top-resistor in series with the probe of ~20 ohms). The maximum bandwidth of the system is 300 kHz. A short straight support was used with a 4 m cable and standard DANTEC straight 55P11 wire. The platinum-plated Tungsten wire is 5μm thick, and 1.25 mm long and has a maximum operating temperature of 300°C. On the other hand, the Platinum/Rhodium (90/10) wire has the same length but is 10μm thick and can be operated up to 800°C. Both wires are welded to two prongs and are sensitive along their entire length. The measurements were conducted at the same locations as the pitot measurements. Table 2 summarizes the test cases measured in the HHK-6 at USAFA.

**Table 2. Summary of test cases**

Reynolds numbers:  $5 \cdot 10^6$ ,  $6.25 \cdot 10^6$ ,  $8.56 \cdot 10^6$ ,  $10 \cdot 10^6$ ,  $12.5 \cdot 10^6$ ,  $16 \cdot 10^6$ ,  $18 \cdot 10^6$   
 Position:  $X = 0, 300 \text{ mm}$ ,  $Z = 0, 25, 50, 74, 100 \text{ mm}$   
 Stagnation Temperature: 410K, 450K, 470K, 480K  
 Instrumentation: SPP PCB, SPP Kulite, Hotwire

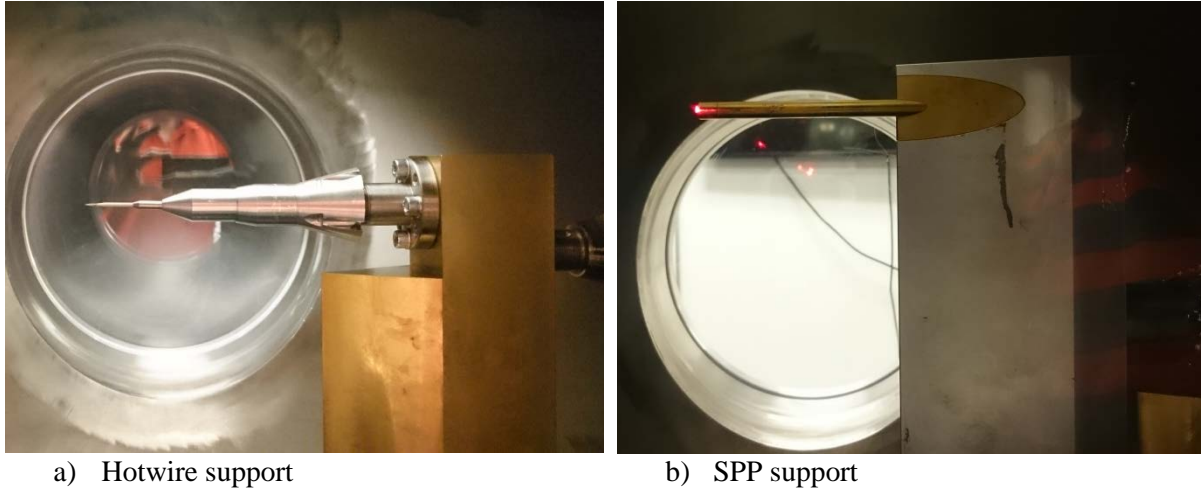


**Figure 3. Freestream characterization, probe holder for vertical position variation**

The hotwire and pitot were moved inside the test section of the wind tunnel using a traverse system. This system consists of two, one-axis components, connected perpendicular to each other allowing the probe to change positions in axial and vertical directions. Figure 3 shows an image of the traverse system holding a) the hotwire probe and b) the stagnation point probe.

### C. Hotwire calibration

The theory to transform voltage fluctuations into flow variable fluctuations is based on the working principle of the anemometer. To address this topic refer to CTA anemometry from Lomas [7], and its specific use in supersonic and hypersonic flows [8]. In the present report, only a short description is given of the method used to connect heat transfer at the wire with velocity, density, and temperature fluctuations. An example of the method implemented here was presented by Smit et al. [9].

The process is divided into two main steps: the calibration and the calculation of the flow fluctuations. The hotwire measures the heat transfer rate between the wire and the surrounding flow. Assuming that the heat exchange is mainly caused by forced convection, a semi-empirical equation can be used to model the heat transfer at the filament,

$$Nu = \frac{H}{\pi k l (T_w - T_e)} = \frac{E^2 R_w}{\pi k l (R_w + R_a)^2 (T_w - \eta T_0)} = X + Y Re^n \quad (1)$$

In this equation,  $H$  is the power loss from a filament with the length  $l$ ,  $T_w$  is the wire temperature, which is spatially averaged,  $T_e$  is the wire recovery temperature, and  $k$  is the heat conductivity of the ambient fluid.  $X$  and  $Y$  are characteristics of the hotwire but depend on the overheat ratio.  $Re$  is the Reynolds number, and the exponent  $n$  depends on the wire operating conditions.

The output voltage depends on the mass flow or Reynolds number and two parameters,  $X$  and  $Y$ , which are constant for a specific wire at a given overheat ratio (OHR) and total temperature. The mass flow exponent  $n$  is determined varying the mass flow and linear fitting,  $E \sim E(\rho u, T_0)$ . One can determine the calibration coefficients by calculating the logarithm derivative of the output voltage with respect to the each sensitive variable:

$$\frac{E'}{\bar{E}} = K_m \frac{m'}{\bar{m}} + K_{T_0} \frac{T_0'}{\bar{T}_0} \quad (2)$$

where  $K_m = \frac{\partial \ln(E)}{\partial \ln(\rho u)}$  is the mass flow sensitivity and  $K_{T_0} = \frac{\partial \ln(E)}{\partial \ln(T_0)}$  is the total temperature sensitivity.

#### D. Hotwire measurements

It is clearly not possible to determine two unknown,  $\frac{m'}{\bar{m}}$  and  $\frac{T_0'}{\bar{T}_0}$ , from only one measurement of  $\frac{E'}{\bar{E}}$ . Additionally, it is not possible to directly work with the time resolved data. Thus, to introduce experimental values in the equation, the equation must be squared and time averaged, see eq. (6), resulting in 3 unknowns. Hence, at least three measurements at three different overheat ratios are required to determine mass flow and total temperature fluctuations.

$$\langle E \rangle^2 = K_m^2 \langle m \rangle^2 + 2 K_m K_{T_0} \frac{\overline{m' T_0'}}{\bar{m} \bar{T}_0} + K_{T_0} \langle T_{T_0} \rangle^2 \quad (3)$$

During the present project two different approaches were investigated, where the flow disturbances are decomposed into acoustic, entropy and vorticity mode. Logan's approach uses the definitions of mass flux and total temperature, combined with the equation of state for an ideal gas to calculate density, velocity, and static temperature fluctuations [10]. Once the variables were obtained, the decomposition of the three modes, namely, the acoustic mode  $\pi$ , the entropy mode  $\sigma$ , and the vorticity mode  $\omega$ , is achieved following Morkovin's definition. Morkovin also proposed another approach where the modal decomposition is directly obtained from the primitive hot wire variables [11]. The two approaches were tested and compared.

## 2.3 Slender Body Experiments

A 7° half-angle cone was specifically designed for the present investigation. The model is composed of five main parts, and has a complete length of 500mm Figure 4. The main body is made from black Plexiglas in order to allow for infrared thermography measurements. The tip, however, is made from steel, since a material with good machining properties is required in order to manufacture very sharp tips. The tip of this model was measured under a laser scan microscope and has a radius of 90μm.

To have the best possible comparison between both wind tunnels, the model was not modified in any way between the measurements in HLB and HHK-6. Only the tip and the base disc were unmounted to ensure that the parts do not suffer any damage during transportation.



**Figure 4. Explosion view of the cone model**

The dominant transition mechanism in low disturbance hypersonic flows is an acoustic wave, which is referred to as second-mode instability. This wave propagates along the surface forming small pressure waves that are modulated by the boundary layer thickness. Due to the eigen function of the mode, pressure sensors are the best choice for detecting and characterizing these instabilities. The model was instrumented with 13 pressure sensors of the type PCB132A31, with a spacing of 25mm, and mounted along a cone ray. At approximately 250mm downstream of the tip of the model, two sensors were installed at the same stream-wise position, but at two different azimuthal angles - one located at  $120^\circ$  and the other one located at  $240^\circ$ . A schematic diagram of the instrumented model is presented in Figure 5.

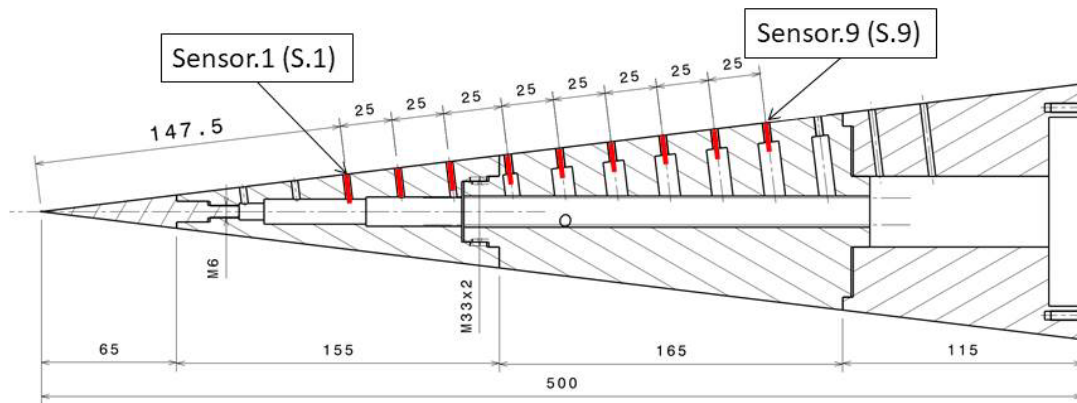


**Figure 5. Section of the cone model with a description of sensors position**

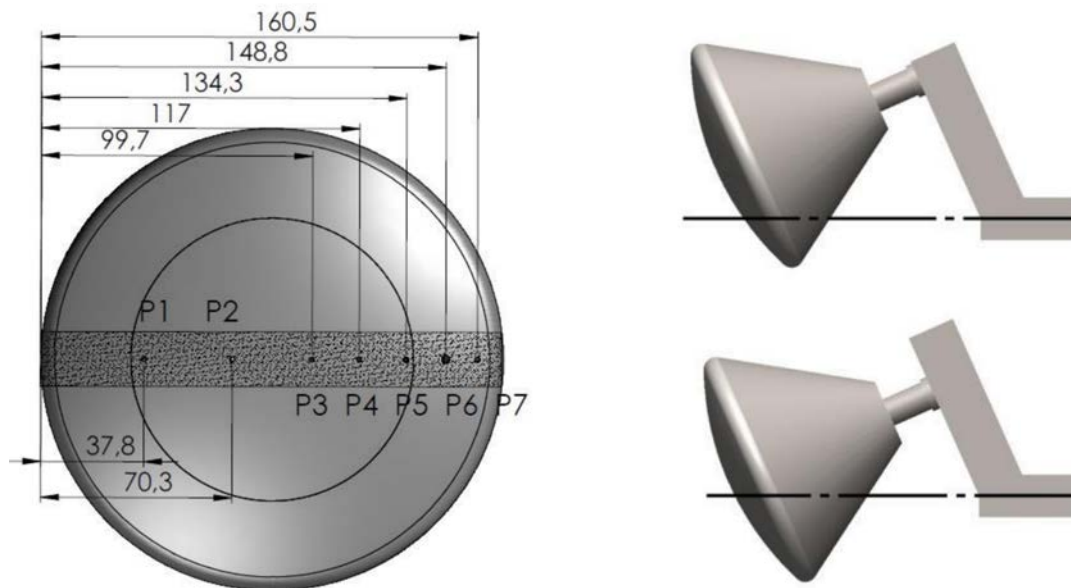
The tests were performed at  $0^\circ$  angle of attack and at nominally Mach 5.9. The angle of attack was set by comparing the signals from the three pressure sensors at different azimuthal positions, and by analyzing the topology of the transition line measured using infrared thermography. A detail of the test conditions is presented in the table below. Since the disturbance level and temperature distribution in the test section is not homogeneous, the measurements were conducted at three different positions along the vertical axis  $z=75\text{mm}$ ,  $z=50\text{mm}$  and  $z=0\text{mm}$  at  $x=0\text{mm}$ .

The transition location was measured by means of infrared thermography. The TU Braunschweig and the USAFA own a middle wavelength range infrared camera (MIR). In the HHK-6 a camera from the FLIR Company capable of recording 60fps (300fps were acquired using a crop sensor configuration) with a maximum resolution of 1280x720 pixels was used. In the HLB a camera from the Infratech Company capable of recording 100fps with a maximum resolution of 640x512 pixels was used. One of the windows of the test section was changed with a sapphire glass. With this setup, a larger section of the model surface could be captured, so there was no need to change positions to capture the transition location for a wide range of unit Reynolds numbers. Table 3 summarizes the flow condition at which the tests were conducted.

**Table 3. Test matrix of cone measurements**

Position x [mm]	Position z [mm]	$p_0$ [bar]	$T_0$ [K]	Re/m [1/m]	AoA [deg]
0	75 50 0	21	480 450 410	1,80E+07	0
		18,68		1,60E+07	0
		14,7		1,25E+07	0
		10		8,56E+06	0
		7,3		6,25E+06	0
		5,85		5,0E+06	0

## 2.4 Blunt Body Experiments



a) Sketch of capsule front with sensor positions

b) Capsule locations with respect to the tunnel axis

**Figure 6. Sketches of the Apollo shaped capsule model mounted in the wind tunnel with 24 deg AoA**

During further measurement campaigns in both tunnels, blunt body experiments were conducted. Previous tests identified the maximum model size that can be used in these facilities. The model used during the present investigations has a diameter of 170mm. To verify that the



wind tunnel is operating correctly and that hypersonic flow is established by all tested conditions, tests were conducted in the HLB using Schlieren for visualization. A qualitative comparison of Schlieren images of the model with numerical simulations had been previously presented in Ali et al. [12]. The model is made of stainless steel and is composed of one center disc and a movable outer disc. For the present investigation, the model was instrumented with seven flush-mounted coaxial type E (chromel-constantan) thermocouples (TE,) MCT 19, from Müller Instruments. The location on the surface of the model where the sensors were located can be observed in Figure 6. Two sensors P1 and P2 were located at the luvside of the model, whereas P3-P7 were located on the leeside. The measurements were conducted at 24 deg angle of attack and at different vertical positions in the wind tunnel. A schematic representation of the wind tunnel support can be seen in Figure 4b. Both wind tunnels exhibit higher noise levels closer to the center axis. By changing vertical positions, the effect of different noise levels on the transition can be investigated. At the reference position, the vertical distance between the center point of capsule and tunnel axis is 37 mm.

Furthermore, Figure 4a displays the location of stochastically distributed roughness elements over the capsule front surface covering the entire distance from the luv- to the leeward side with a width of 30mm. The stochastically distributed elements were generated by evenly distributing 100 $\mu$ m spherical particles of polyamide (Vestosint®). On a clean surface, the transition was not observed in the HLB up to  $Re/m = 22 \cdot 10^6$ . To investigate roughness induced transition, a stochastically distributed roughness was applied on the surface.

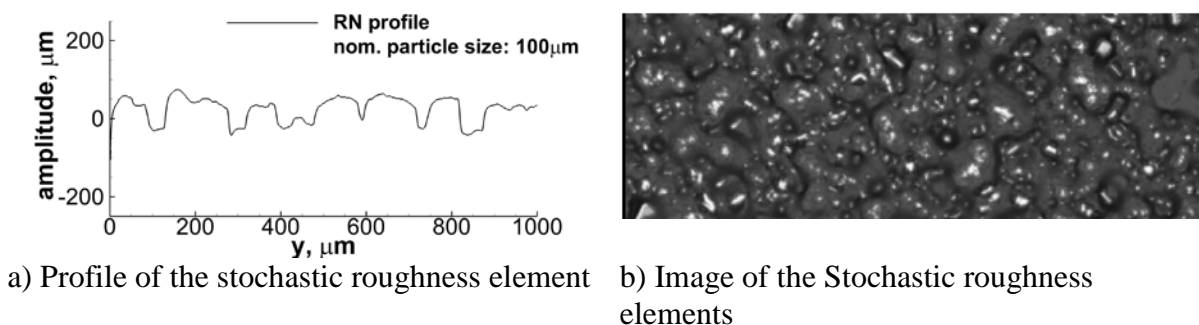


**Figure 7. Analysis of the stochastic distributed roughness element by means of a laser scan microscope**

The height of the stochastically distributed roughness element inside the patch was determined as described by Leidy et al. [13]. The surface roughness was measured in several places, over a small window with a size of 1.4 x 1.4mm, using a laser-scan microscope (Keyence VK-X100K). Five roughness profiles were extracted in streamline direction from each scanned window, each covering approximately five peaks/valleys. The profiles were manually positioned such that large peak-to-valley values were precisely captured. The 30% exceedance criterion was applied on the measured peak-to-valley heights for the data of each scan to obtain numerical k-values [14]. Finally, the k-values for different surface scans were averaged. As a result, the roughness patch with small particles is characterized by a kvalue of 101 $\mu$ m. Note that this value is measured before any wind tunnel testing. During testing, the roughness patch is subject to sandblasting effects of the high-speed air and some random particles crashing into the surface. This effect causes an unintended degradation of the roughness element. This problem cannot be overcome, and for this reason, the effectiveness of the roughness patch is verified by repeating previous measurements after several shots. As a consequence of this degradation, a new roughness patch was generated before conducting experiments in HHK-6.

Although the application of the roughness patch is done manually, the procedure delivers repeatable results. The patch used in HHK-6 was measured using the same procedure as for the HLB, and the roughness patch was characterized by a k-value of  $103.5\mu\text{m}$ . Note that the k-values are determined before conducting wind tunnel tests. During the measurements, the roughness patch is subject to the sandblasting effects of the high-speed air containing dust particles. An unintended degradation of the roughness elements is inevitable. The effectiveness of the roughness patch is proven by repeating previous measurements after several shots.

Special attention was paid to the implementation process of the roughness patch. After covering the thermocouples, black paint was sprayed on the surface to generate an adhesive layer of almost constant thickness. Next, particles were uniformly distributed on the adhesive layer by using a trickle device. After the paint was dried, non-bonded particles were removed. Finally, another layer of paint was applied to enclose the particles. For the measurements, the thermocouples are uncovered, and the local steps caused by the paint around the sensors as well as along the lateral boundaries of the roughness patch were carefully sanded to get a smooth connection between the roughness patch and the clean surface.

## 3 Results and Discussion

### 3.1 Freestream Characterization

#### 3.1.1 Pitot measurements

To compare the noise levels of both wind tunnel, the RMS values of the pressure fluctuations were computed from the signal obtained from the PCB sensor. One has to emphasize that in both wind tunnels the same measurement chain, with the same sensors and signal conditioners, was used. To compute the RMS values, the signal was filtered between 5 to 100 kHz. The comparison of the normalized pressure fluctuations between the two facilities for different  $Re/m$  is shown in Figure 8. The pressure fluctuations were normalized by the mean stagnation pressure on the sensor ( $\langle SPP \rangle = p_{rms}/p_{mean}$ ). The mean value used to normalize the pressure fluctuations was obtained from further measurements with an absolute pressure sensor (Kulite) mounted on the same probe.

Subfigure a) shows measurements at several locations. Although both wind tunnels have similar pressure fluctuations levels at very low unit-Reynolds numbers, significant differences appear as  $Re/m$  increases. While the noise level generally decreases with the Reynolds number in HLB, the behavior is different in HHK-6, causing an important difference in the fluctuation levels at  $Re/m = 10 \cdot 10^6$ . At high  $Re/m$  the noise levels of both wind tunnels become similar again.

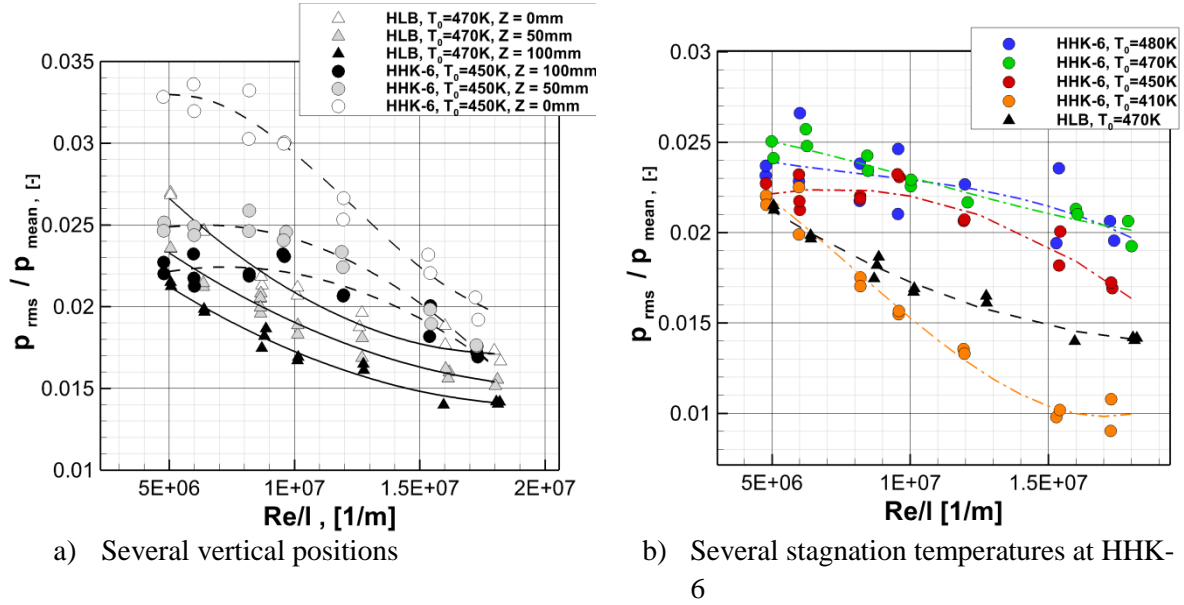


**Figure 8. Normalized values of RMS pressure fluctuations filtered between 5 kHz and 100 kHz**

In both wind tunnels the noise level increases towards the center axis where it attains its maximum value. The higher level of pressure fluctuations at the center of the wind tunnel has two origins. On the one hand, both tunnels are of circular cross-section and have axisymmetric nozzles. The Mach waves that are radiated from the turbulent boundary layer of the nozzle interact at the center line, generating increased pressure fluctuations there. On the other hand, the flow around the fast acting piston that activates the tunnel and separates the high-pressure section from the low-pressure section has a turbulent wake with increased vorticity levels close to the center axis. In all measured cases, the HHK-6 shows higher pressure fluctuations levels, especially when comparing the values at the center line.

Notice that during the measurements the stagnation conditions in both wind tunnels were set equal. Nevertheless, the difference in the construction, storage tube diameter and the location at which the temperature is measured result in slightly different stagnation conditions for the same pre-shot setup. For this reason, the measurements at different positions in USAFA and HLB do not have the same total temperature.

The effect of the tunnel temperature was investigated in the USAFA wind tunnel at the reference position,  $z=100\text{mm}$ . The total temperature was varied from 410K to 490K. At each temperature, several data points at several  $\text{Re}/\text{m}$  were measured. The noise level changes with the total temperature of the flow. If the total temperature is increased, the pressure fluctuations also increase. This increment is so high that the noise level is more than two times higher for  $T_0 = 470$  at  $\text{Re}/\text{m} = 15 \cdot 10^6$  compared to the value at  $T_0 = 410\text{K}$ . It is also of interest that the behavior of the two wind tunnels is similar for very low total temperatures in the USAFA facility. The measurements in HKK-6 show significant run-to-run differences. Particularly high scatter is observed at the maximum temperature. This could indicate that longer waiting times are required for the flow temperature to become uniform in the storage tube.

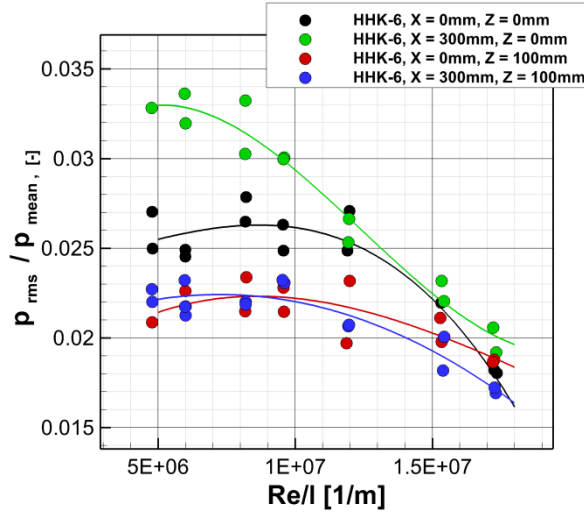


**Figure 9.** Pressure fluctuation for different axial positions in HHK-6 at  $T_0=450\text{K}$  from PCB sensor, filtered between 5kHz to 100kHz

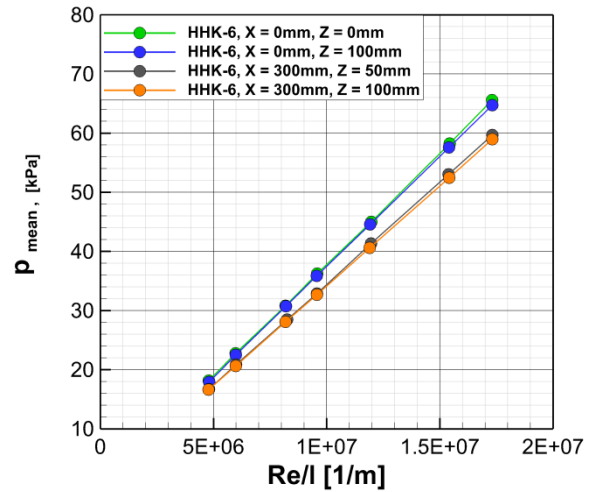


**Figure 10.** Variation of the stagnation pressure along the test section of HHK-6 for  $T_0=450\text{K}$

Additionally to the measurements in the middle of the test section, measurements were conducted at different planes along the tunnel axis. Figure 9 shows the results of the pressure fluctuations at the nozzle outflow ( $X = 0\text{mm}$ ) compared to the pressure fluctuations found in the middle of the test section ( $X = 300\text{mm}$ ). The noise level at  $Z=100\text{mm}$  does not vary considerably over  $X$ . The difference in the fitted curves remains within the scatter of the measured values. Nevertheless, the comparison of the pressure fluctuations along the tunnel center axis reveals a remarkable increment of the noise levels when moving downstream away from the nozzle outflow plane. This increment suggests that the Mach waves from the nozzle are the origin of high noise levels at the center axis. As observed previously, the noise levels found at the center axis are generally higher than those found 100mm above the center.

Also, Kulite sensors were used to conduct measurements at the two axial positions. The wind tunnel nozzle has an opening angle of  $3^\circ$  at its end, which results in a slight flow expansion along the test section. The measurements in Figure 10 show a minor expansion of the flow downstream of the nozzle exit plane. The expansion causes the Mach number to increase inside the test section. The increment of the Mach number can be evaluated based on the relation between  $P_{T2}$ , the stagnation pressure behind the pitot probe shock wave, and  $P_{T1}$ , the stagnation pressure of the incoming flow. The former one is extracted directly from the calibrated Kulite sensor while the latter is computed using the storage tube flow conditions and gas dynamic expansion relations. The results of the measurements at HHK-6 based on the mean pressures are presented in Figure 10.

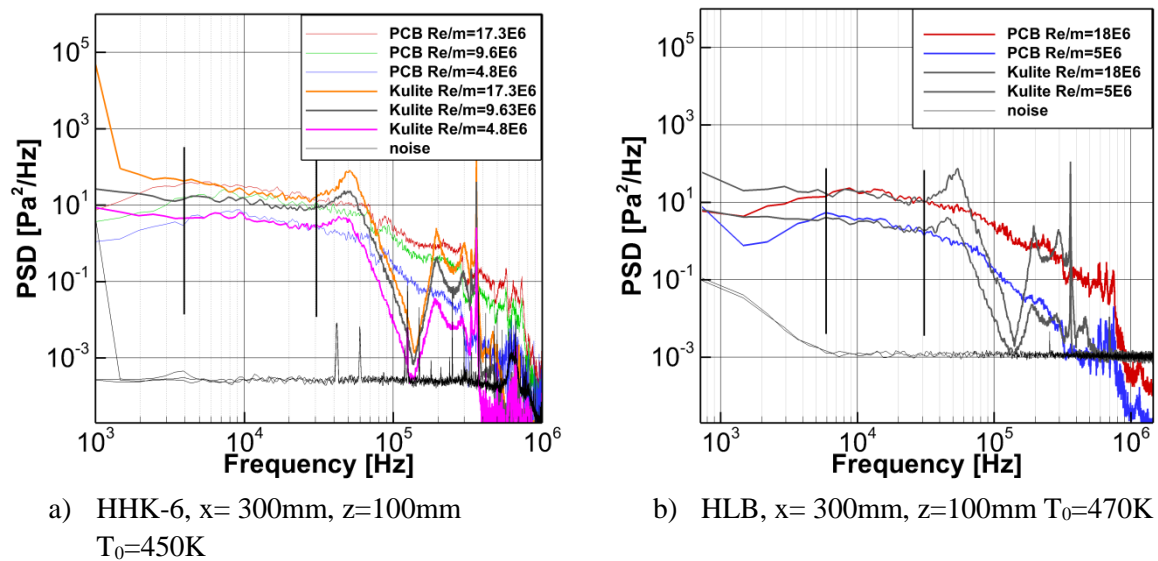


**Figure 11. PSD of pressure fluctuation obtained from PCB and Kulite sensors**

The  $p_{\text{rms}}$ -values of the pressure fluctuations presented were obtained with a PCB sensor. This sensor measures fast pressure fluctuations very accurately, but does not function at low frequencies. For this reason, several measurements were repeated with a Kulite absolute pressure transducer. The absolute pressure sensor was used to measure the mean pressure used to normalize the pressure fluctuations, and also to measure absolute pressure fluctuations for a specific frequency range. Figure 11 shows the comparison of the pressure fluctuations obtained with a Kulite and a PCB sensor. An excellent agreement between the sensors is observed for frequencies between 5 kHz to 30 kHz in both facilities. This agreement is maintained during the entire Reynolds number range. Below 5 kHz the PCB sensor shows a considerable attenuation of the signal. An overshoot in the pressure amplitude is measured by the Kulite around 50 kHz. This peak varies in amplitude with the Reynolds number and is caused by the resonance of the air inside the cavity of the sensor. For higher frequencies, a high decay in the pressure fluctuations is observed until they equal the noise level. The sharp peaks seen beyond this point correspond to the resonance frequency of the sensor itself.

### 3.1.2 Hotwire Measurements

The hotwire measurements were performed using the same setup in both wind tunnels. Exemplary time traces of sensor signals at the reference location and  $Re/m = 10 \cdot 10^6$  are displayed in Figure 12. The figure shows the output voltage of the hotwire system for two different total temperatures in the HHK-6 and one temperature in HLB. The signal is characterized by its pre-run voltage, a sharp peak corresponding to the tunnel starting shock, a more flattened region during tunnel run time, followed by a high noise level during the breakdown of the hypersonic flow. It can be observed that both wind tunnels present approximately 100ms seconds of running time, which is slightly longer in the USAFA facility than in HLB. For flow conditions during the run one would expect constant mean values of the signal over time. However, in both facilities, decay in the mean voltage is observed during the run. Further tests without heating showed that the variation of the voltage output of the hotwire can be related to the variation of the stagnation temperature during the run. This variation is higher in the HHK-6 facility than in HLB. This effect is also observed for runs at different temperatures.

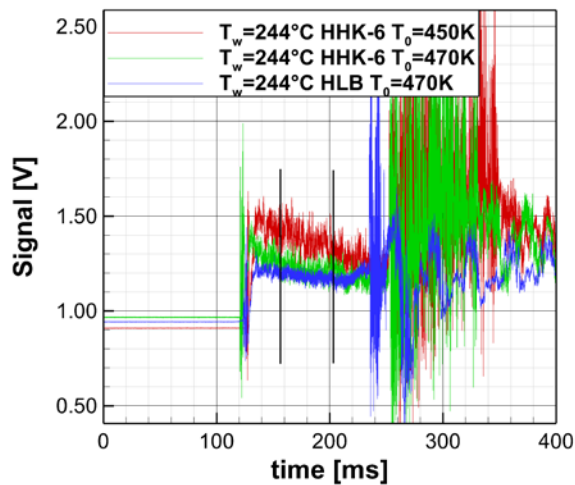


**Figure 12.** Time traces of hotwire measurements in HLB and HHK-6 at the reference position and  $Re/m=10 \cdot 10^6$

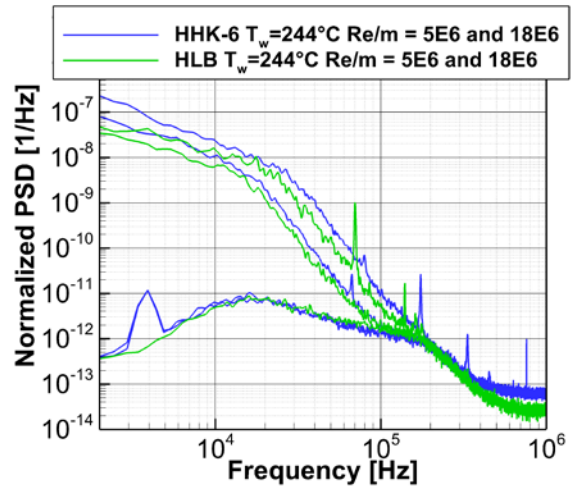


**Figure 13.** PSD of the output voltage of the  $5\mu m$  hotwire, in HLB at  $T_0=470$  and HHK-6 at  $T_0=450$  and same wire temperatures, normalized by the mean voltage

An inspection of the hot wire signals in the frequency domain is presented in Figure 13. The comparison shows very similar amplitudes in the complete spectral domain, indicating maximum resolved frequency of about 100kHz. A distinct slope change above 30kHz is observed. Also, a sharp peak around 70kHz is found by the highest  $Re/m=18 \cdot 10^6$  in the HLB. This peak can be considerably reduced by gluing the prongs of the probe.

A square wave test was conducted in order to obtain the best setup of the hotwire system. The maximum frequency resolution is calculated based on the 97% decay criteria or the -3dB amplitude loss in the frequency domain. Both methods delivered very similar results. The results of the  $5\mu m$  Platinum-plated tungsten wire at  $Re/m=10 \cdot 10^6$  and different OHR showed a response of around 100 kHz. This value varies with the wire temperature and the flow conditions. Using the same set up and the same wire in the HLB, a different frequency response was obtained (approx. 65kHz). The difference is most likely caused by differences in flow temperature and density between both wind tunnels. Furthermore, in order to overcome the temperature limitations of the Platinum-plated tungsten wire ( $300^\circ C$ ), a Platinum/Rhodium (90/10) wire of  $10\mu m$  diameter was employed. This can be used at temperatures up to  $800^\circ C$ . The drawback of the sensor is the larger diameter. As can be seen in Figure 14 the thicker wire results in a lower frequency response of about 30kHz. Despite of the differences of the square wave tests, similar frequency decays between the two wires are obtained during the run, see Figure 15. It appears that both wires resolve flow fluctuations up to 100kHz, while they indicate a change in the slope beyond 30kHz for the  $5\mu m$  wire and 20kHz for the  $10\mu m$  wire.

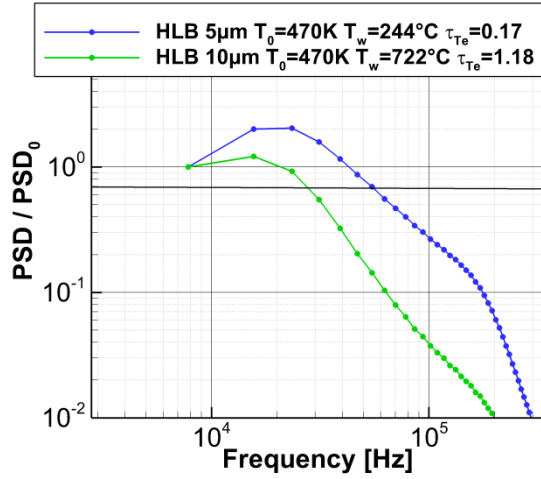


**Figure 14.** Square wave test of the 5μm and 10μm wires signal in HLB at  $Re/m=10 \cdot 10^6$

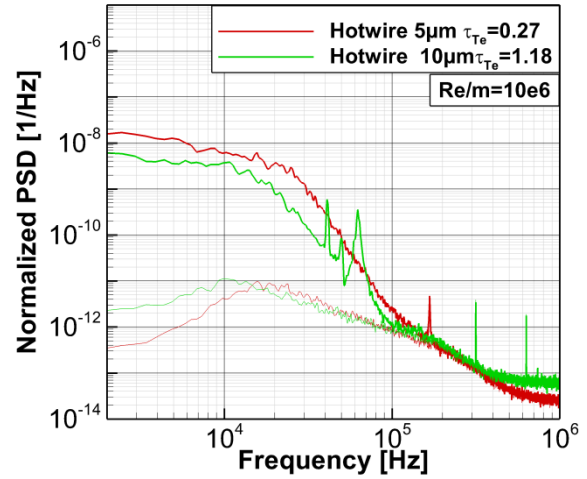


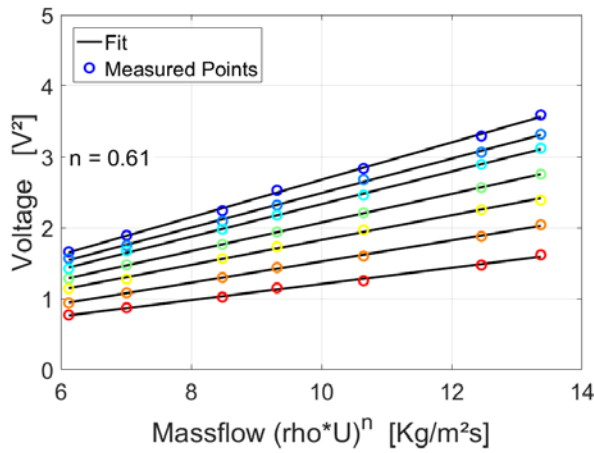
**Figure 15.** PSD of the output voltage between the 5μm and 10μm hotwires in the HLB at  $Re/m=10 \cdot 10^6$

### A. Hotwire Calibration

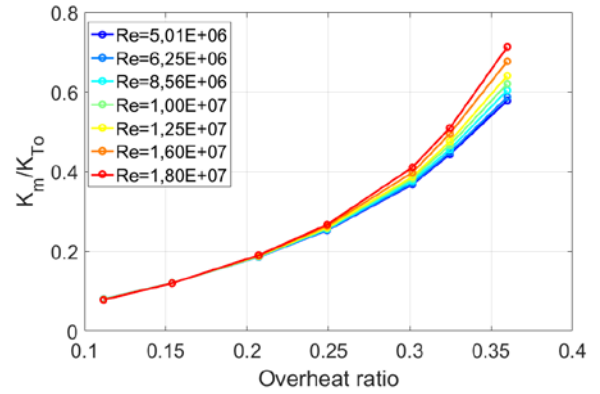
The first step in order to carry out modal analysis by means of hotwire consists of calibrating the system by computing the sensitivities coefficients. An in-situ calibration was performed in the present work for each wind tunnel. The calibration is carried out following the equation presented above

$$E^2 = L + M (\rho u)^n \quad (3)$$

As mentioned, L and M are functions of the overheat ratio and the total temperature. By running the CTA system at different overheats at the same incoming flow condition a linear relation of  $E^2 \sim (\rho \cdot u)^n$  is obtained. By running the tunnel with different total pressures but at constant total temperature, the relation between the Nusselt number and the Reynolds number is established, namely the output voltage and the mass flow relation as shown in Figure 16. The best linear fit is obtained with a Reynolds number exponent of 0.61.



a) Fitting of  $E^2 \sim (\rho \cdot u)^n$



b) Sensitivity coefficients relation

**Figure 16.** Determination of the best coefficient for the linear fitting of  $E^2 \sim (\rho \cdot u)^n$



The relative sensitivities of hotwire with respect to mass flow and total temperature can be deduced from the calibration. Figure 16b shows that the hotwire is more sensitive to mass flow at higher overheat ratio, whereas it is more sensitive to total temperature at low overheat ratio.

## B. Results of Hotwire Measurements

Hotwire measurements were conducted in both facilities using the 5 $\mu$ m wire. The comparison of the mass flow fluctuations and the total temperature fluctuations is presented in Figure 17. Although both wind tunnel show similar levels of total temperature fluctuations, the mass flow fluctuations measured in HHK-6 are more than twice as large than those measured in HLB.

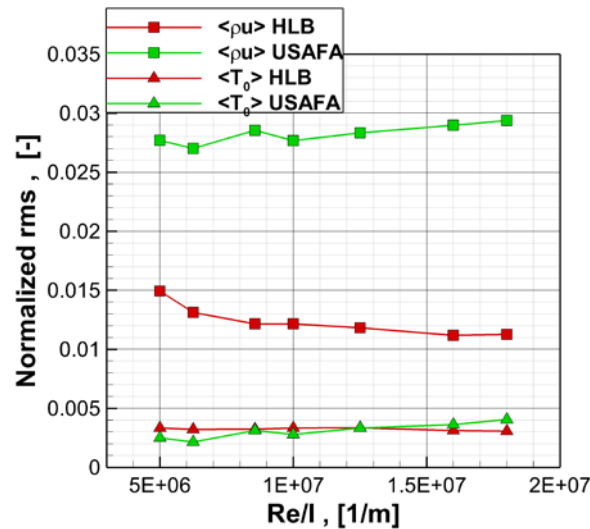


**Figure 17.** Mass flow and total temperature fluctuations in HLB and HHK-6 from filtered signals between 5 and 100kHz with the 5 $\mu$ m wire

The mass flow and total temperature fluctuations found with the 10 $\mu$ m wire are presented in Figure 18 and Figure 19, as a comparison of the values obtained with both, 5 and 10 $\mu$ m wires for two frequency bands. The 10 $\mu$ m wire measures higher total temperature and mass flow fluctuations in both frequency intervals. While decrease with unit Reynolds number is expected for all measurements, increased values found in mass flow fluctuations with the 10 $\mu$ m wire for 5 to 100kHz appears to be caused by the peaks above 30kHz found in the data, see Figure 15. Note, that similar peaks had been found with the 5 $\mu$ m wire. Gluing the prongs with two components epoxy resin solved the problem for the thin wire but not for the 10 $\mu$ m wire.



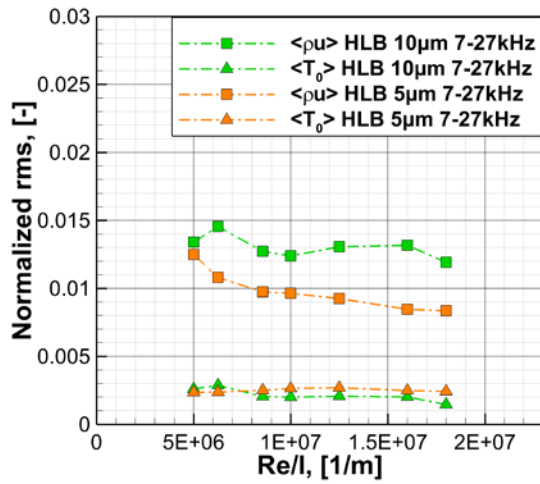


**Figure 18. Effect of wire on mass flow and total temperature fluctuations in HLB at  $T_0=470K$ ,  $x=300mm$  and  $z=100mm$**

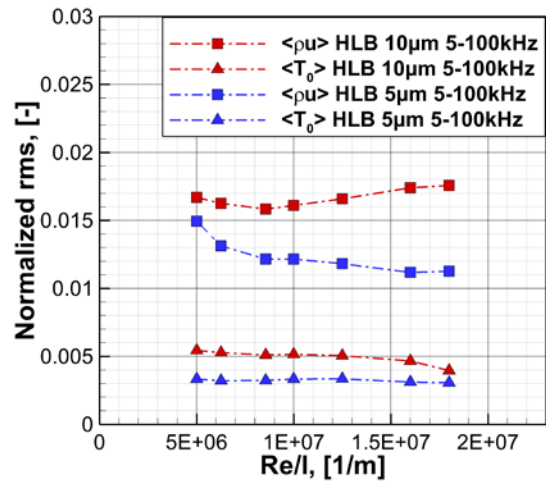


**Figure 19. Effect of wire on mass flow and total temperature fluctuations in HLB at  $T_0=470K$ ,  $x=300mm$  and  $z=100mm$**

The results of our hotwire measurements revealed quite some uncertainties in the results, related to using different wires, calibration methods and filtering the measured time traces. Therefore, it appears very useful to compare the measured hotwire data to DNS simulations of the wind tunnel flow. For this purpose, one numerical set of data exists, where the acoustic waves generated by the hypersonic nozzle boundary layer of the HLB-facility were simulated by Duan et.al. [15]. Note that this DNS did not include the effects of entropy fluctuations and vorticity fluctuations in the inflow to the HLB-nozzle, as Duan et al assumed that the test section flow would be dominated by acoustic disturbances. This DNS data, albeit available for the relatively low unit Reynolds number of  $6.25E06$  only, is used here to assess the present hot wire measurements in HLB. Figure 20 shows the comparison of the measured mass flow and total temperature fluctuations and results from the DNS simulations for three different axial locations in the test section. Note that the numerical RMS-values are obtained from unfiltered time traces. Fair agreement between the measured values and the results of the DNS simulation is observed. The larger numerical RMS-values stem from not filtering the numerical data. As time traces of the numerical data were available only for  $x=0mm$  (entrance to the test section), these time traces were used to obtain filtered RMS-values of numerical data. Figure 21 shows that filtering reduces RMS-values of mass-flow fluctuations and temperatures by a certain factor. In the following section, we assume that the effect of band-pass filtering on numerical RMS-values can be represented by a fixed scaling factor, to be applied at other locations in the test section as well. This assumption is obviously valid, as long as the spectra at other locations in the test section exhibit similar amplitude distributions in the frequency domain.

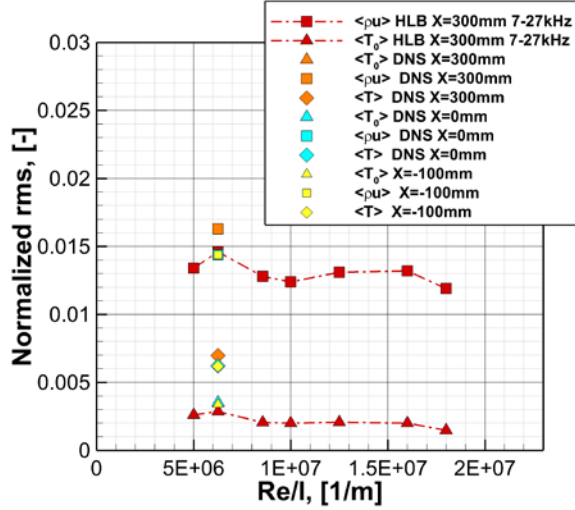


**Figure 20. Comparison of mass flow and total temperature fluctuations between DNS simulation and experimental data in HLB at  $T_0=470\text{K}$  at  $x=300\text{mm}$  and  $z=100\text{mm}$**

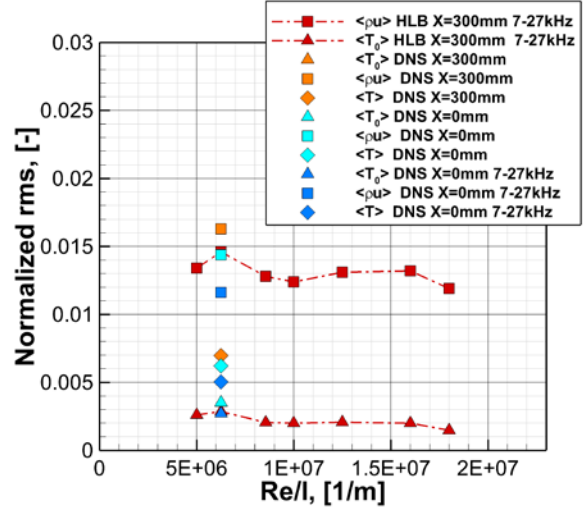


**Figure 21. Filtered DNS simulation at the outflow plane of the nozzle compared to filtered data from the measurements in HLB.**

### C. Reconstruction of Freestream Disturbances and Modal Decomposition

For characterizing the nature and origin of freestream disturbances in the high-speed wind tunnel, two modal decomposition methods were implemented. These approaches decompose wind-tunnel freestream disturbances into three modes of co-varying physical properties. These modes represent an acoustic or sound-wave mode, (isentropic variation of pressure, density, and temperature as well as that of the coupled irrotational velocity field), an entropy mode (isobaric variation of entropy, density, and temperature, also described as entropy or temperature spottiness), and a vorticity mode (variation of the solenoidal component of the velocity field).

The proposed methodologies use the concept of so called combined modal analysis. This means the information of more than one probe is combined for modal decomposition. Both proposed methods require the amplitude of the static pressure fluctuations and this is one of the critical variables in the analysis. Logan utilized separate static pressure fluctuation obtained by means of laser-induced fluorescence (LIF) [10]. Stainback and Wagner introduced a rather simple approach for relating pre-shock static and post-shock total pressure fluctuations of a pitot probe [16]. Another simulation-based approach for stagnation point probes (SPP) was introduced by Schilden and Schroeder [6]. This decomposition method uses total pressure fluctuations and stagnation point heat fluxes to decompose freestream disturbances via a sensitivity matrix, which contains transfer functions between the measured quantities and acoustic and entropy modes in the freestream. The transfer function between post-shock measured stagnation pressures and pre-shock pressure fluctuations is defined as follows:

$$\frac{r_{ac}^2}{\gamma^2} \langle p_{ac} \rangle^2 + r_{en}^2 \langle T_{en} \rangle^2 = \langle SPP \rangle^2 \quad (4)$$

where  $r_{ac}$  and  $r_{en}$  are the coefficients of the transfer matrix,  $\langle SPP \rangle$  denotes the pressure fluctuations measured by the probe, and  $\langle T_{en} \rangle$  are the entropy fluctuations in the freestream.

The coefficients of the transfer function of the DNS depend on the frequency and the angle of the incidence waves. Relevant for the present case is the frequency 17kHz as provided by Ref. [6]. Here, the transfer coefficient has a value of 0.5195. For this reason, the experimental data was band-pass filtered as already defined above,  $17\text{kHz} \pm 10\text{kHz}$ .

The low values of the entropy fluctuations combined with high conditioning number of the set of decomposition equations make the inversion of the matrix combining Schilden's DNS with Logan's decomposition approach difficult. Therefore, the static pressure fluctuations of the present work were computed assuming that the entropy fluctuations were small in comparison to freestream pressure fluctuations so that the contributions of entropy variations on pitot pressure fluctuations are negligible. Figure 22 and Figure 23 show a comparison between the mass flow, total temperature, pitot pressure fluctuation, and reconstructed freestream pressure fluctuations for unfiltered and filtered DNS data, respectively. Very good agreement between the results of the filtered numerical simulation and the measured data is obtained for static freestream pressure fluctuations, mass flow fluctuations and total temperature fluctuations. As the fluctuations of the flow variables in the DNS simulations are solely originated in the turbulent boundary layer of the nozzle of the wind tunnel, we conclude that the fluctuations coming from the storage tube are indeed small in comparison to the fluctuations originated in the boundary layer of the nozzle.

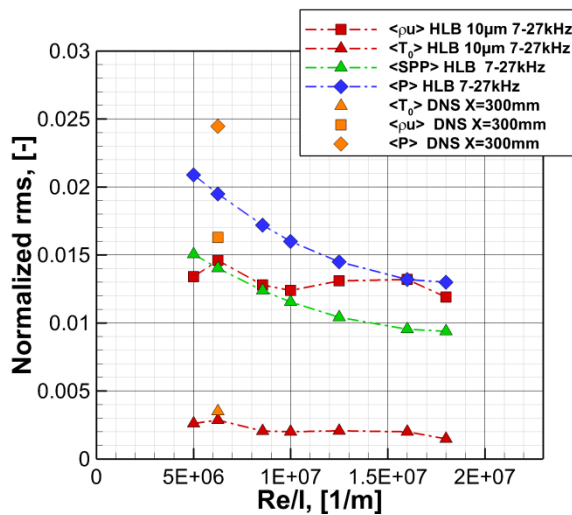


**Figure 22.** Mass flow, total temperature, and pressure fluctuations of DNS and filtered experimental data for  $T_0=470\text{K}$  at  $x=300\text{mm}$  and  $z=100\text{mm}$

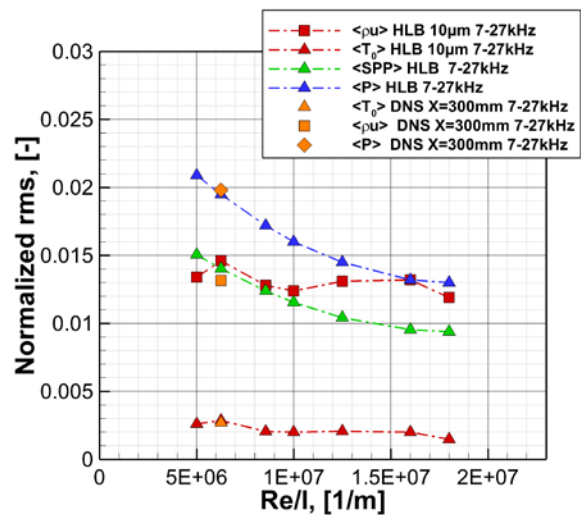


**Figure 23.** Mass flow, total temperature, and pressure fluctuations of filtered DNS and experimental data for  $T_0=470\text{K}$  at  $x=300$  and  $z=100\text{mm}$

Before calculating the modal disturbances with Logan's approach, the different flow variables are computed. A comparison of the results with DNS data is shown in Figure 24. Similar static temperature fluctuations as those seen found in the DNS simulation are obtained in this case. However, the velocity fluctuations are represented by imaginary numbers while the density fluctuations are slightly overestimated. This results in a modal decomposition with unphysical, imaginary numbers for vorticity.

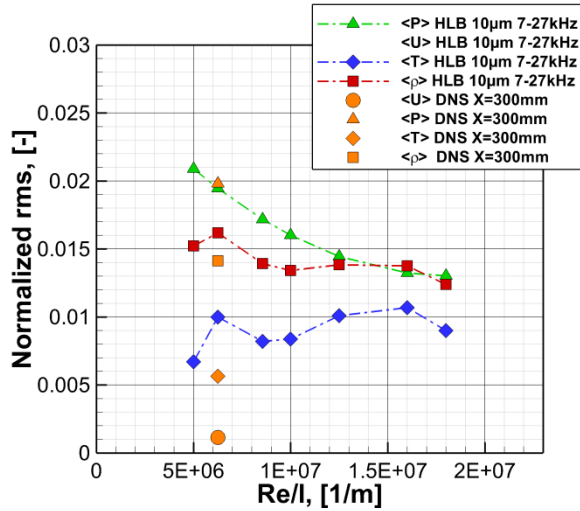


**Figure 24. Freestream temperature, velocity, density and pressure fluctuations computed following Logan's approach compared to DNS data**

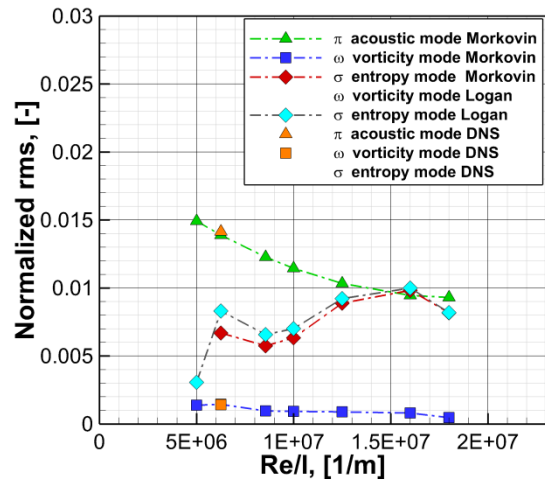


**Figure 25. Modal decomposition of freestream disturbances in HLB for Logan and Morkovin approaches**

Markov's decomposition method delivers proper vorticity values, but it also results in rather high entropy fluctuations, which are very sensitive to small changes in the mass flow fluctuations. In order to validate our application of Markov's methodology, the same analysis was conducted using the mass flow, total temperature and pressure fluctuations provided by the DNS simulation. We noticed that small changes of mass-flow fluctuations from the DNS, relative to the hotwire as i.e. displayed in Figure 23, result in substantial changes of the entropy mode. Furthermore, at lower Reynolds numbers the measured, combined probe data, as well as the analysis of the numerical data, result in nonphysical imaginary numbers for entropy fluctuations in the order of E-3. Therefore, we computed entropy fluctuations of the DNS data directly from the time-resolved data. In this case, positive values of the entropy mode resulted in the order of E-5, which corresponds well to the expectation for a flow field of purely acoustic waves.

We note that both modal decomposition methods investigated here are based on the physical model of an ideal gas considering small perturbations. In order to use experimental values, the equations have to be squared and time averaged. By doing so, correlation coefficients between different variables need to be modeled. Logan tries to solve the problem by assuming that Mach waves are uncorrelated to the other modes. Our comparisons with DNS data indicate that Logan's model is not valid for wind tunnel freestream flows with low levels of entropy and vorticity modes relative to the acoustic waves. Applying Morkov's method has the advantage that the data directly extracted from the hotwire can be combined with the pressure fluctuations to decompose the flow disturbances. Although the method seems to work better and has a lower condition number when inverting the matrix, also negative entropy values may be obtained when entropy fluctuations are small in comparison to pressure fluctuations, hence the method is also not robust.

A more detailed study of the correlation between the different modes needs to be conducted in order to develop a method that can reliably reconstruct freestream disturbances based on combine data from hotwire and stagnation point probes.

## 3.2 Cone Measurements

The 7° half-angle cone models have been widely used in the past to study transition mechanisms and the receptivity process. Special attention to the latter is paid in the present study. The receptivity process defines how external disturbances enter the boundary layer, and modal instabilities are formed. The receptivity is affected by many factors such as surface roughness, noise level, type of external disturbances, and strength of the shock wave, to name a few. Thus, it is difficult to develop algorithms capable of predicting the transition location, even when the dominating transition mechanism is known. Comparing transition on the same model between two facilities where the free stream disturbances are thoroughly characterized gives more reliable results and a better basis to understand the effect of the noise on transition, and provides a set of data by which different wind tunnels can be compared.

The second-mode instability was studied by means of PCB pressure transducers. An analysis in the frequency domain of the signals is very useful to detect and characterize the instabilities. Figure 26a shows the power spectral density of the second mode instability measured at model position  $x=0\text{mm}$  (tip of the model at nozzle outflow plane),  $z=75\text{mm}$ , and  $Re/m=8.56E6$  in HHK-6 at USAFA and HLB at TU Braunschweig. The second mode instability appears in the frequency domain as a relatively sharp peak at high frequencies between 200kHz and 500kHz approximately. As expected, the second mode is unstable and it grows downstream, as can be observed comparing the amplitude of the second mode peak from sensor S.1 to sensor S.9. The coupling of the second mode to the boundary layer thickness is responsible for the frequency shift of the peak observed when comparing the sensors. The thickening of the boundary layer results in a decrease in the frequency at which the most unstable mode is found.

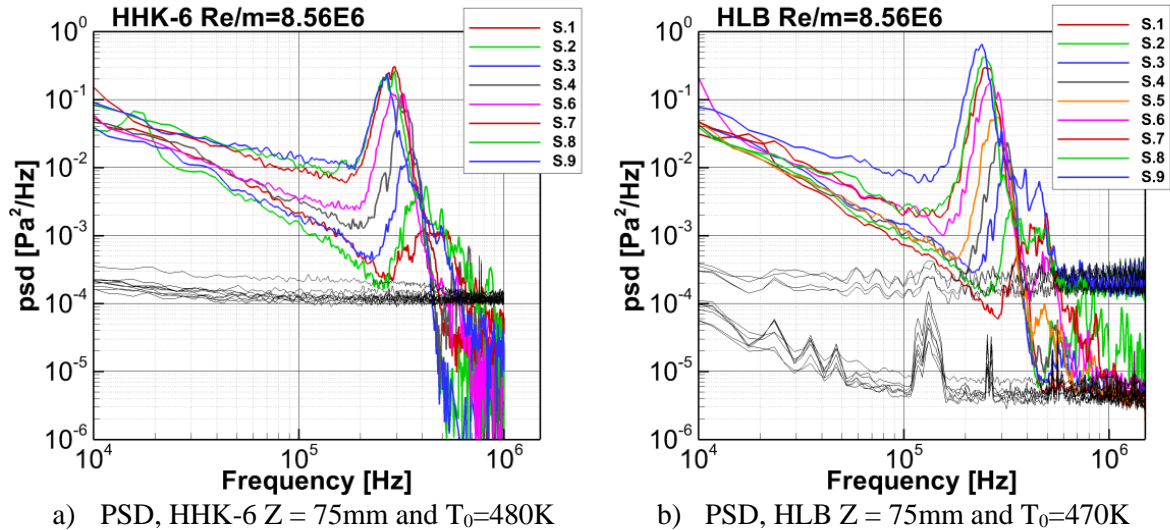


**Figure 26. Power density spectra of pressure fluctuations on the surface of the 7deg half angle for two locations in the HHK-6 at  $Re/m=8.56E6$**

The analysis of the second mode instability was conducted for seven different Reynolds numbers giving a good map of the behavior from early stages of transition up to its breakdown into turbulence. When comparing the results obtained in both wind tunnels, some significant differences are noticed. Figure 26b shows the amplitude of the second mode instabilities for the same Reynolds numbers, but a slightly lower total temperature (10K). The measurements in HLB display sharper second mode peaks and larger amplitudes compared to the ones obtained

in HHK-6. When the model was mounted in the HLB with lower disturbances levels, the first sensors registered lower amplitudes of pressure fluctuations. At higher Reynolds numbers further downstream on the surface, the opposite occurs. The second mode peaks achieve higher amplitude and saturate later than in the HHK-6. The effect of the noise level on the second mode instability was investigated in detail in the HHK-6.

The measured data is evaluated based on the assumption that the cone was exactly aligned with the flow. A misalignment can have a strong influence on the transition. For this reason, special attention was given to the yaw and pitching angles. If the cone is perfectly aligned with the flow, transition will occur at the same axial location along the entire surface of the model. As a result, a straight transition line (perpendicular to the cones axis) is obtained. In this case, infrared thermography was used not only to detect transition location, but also to set the zero degrees angle of attack. In addition to this method, three PCBs sensors were mounted with  $120^\circ$  azimuthal angle variation at the same axial location. In this way, the amplitude of the second mode instability could be compared. A misalignment of the cone with the incoming flow will cause a shift in the frequency and the amplitude at which the peak of the most unstable mode appears. A result of this analysis can be seen in Fig. 28 a). A small disagreement of the peaks is visible at the reference position for  $Re/m = 8.56E6$ . This difference varies with the Reynolds number, being in some cases smaller and in some cases slightly larger. By rotating the cone along its main axis the circumferential position of the sensors with respect to the free stream can be varied without changing the angle of attack. This adjustment is possible because the model can be decoupled from the supporting disc which is responsible for fixing pitch and yaw angles. The results of rotating the cone 90 degrees in counterclockwise direction are shown in Fig. 28 b). No difference in the frequency range of the second mode peak can be observed between the three sensors. This result verifies that the boundary layer thickness is the same, and therefore shows no evidence of model misalignment. The disagreement observed is most likely caused by a non-uniform distribution of the disturbances of the incoming flow in the test section. Similar results were observed in HLB. In this case, although the transition appears as a straight line, the sensors showed the same behavior as in HHK-6.

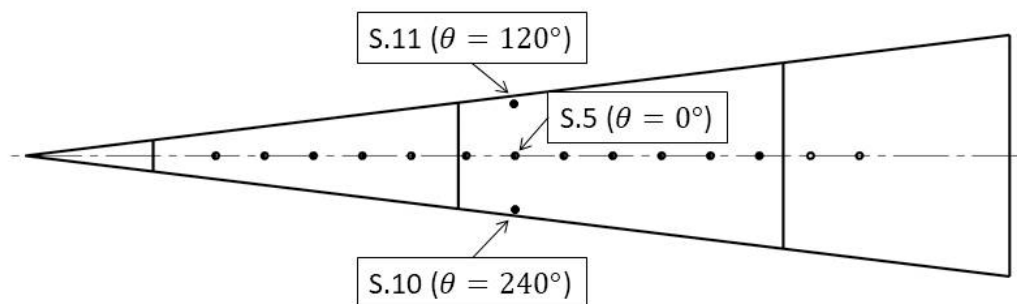
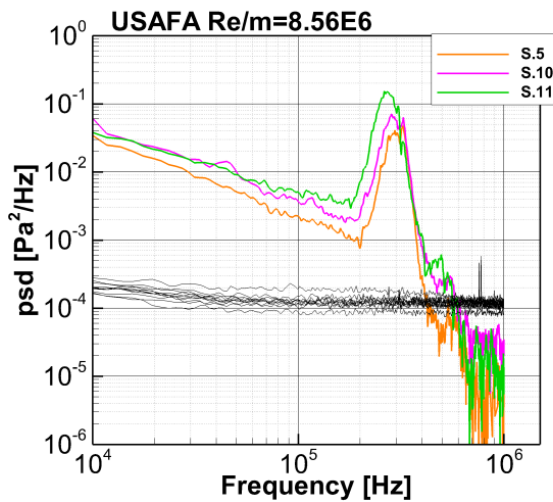
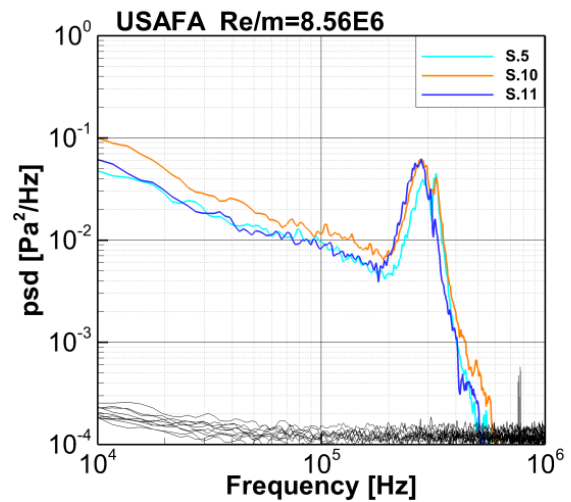


**Figure 27. Sketch of sensors location distributed in azimuthal direction at the same axial location**





a) Reference test case,  $T_0 = 450K$



b) Rotated 90°,  $T_0 = 410K$  and  $Re/m=8.56E6$

**Figure 28. Power density spectra analysis of pressure fluctuations of three sensors distributed in azimuthal direction at the same axial position in HHK-6 at  $z=75mm$**

Complementary to the measurements at  $z=75mm$ , measurements were conducted at several Reynolds numbers and at two additional vertical positions in the test section. A comparison between the reference position ( $z=75mm$ ),  $z=50mm$ , and the center axis of the wind tunnel ( $z=0mm$ ) can be seen in Figure 29a-d for different unit Reynolds numbers.

The effect of the fluctuation level on the second mode is presented in Figure 29 in the frequency domain based on the signal of sensor S.5. At lower Reynolds numbers, higher initial amplitudes in the entire frequency domain are observed. The maximum amplitude of the second mode peak remains constant. Thus, much higher relative maximum amplitudes are obtained at  $Z=75mm$ . Increasing the Reynolds number increases the amplitude of the second mode instability and reduces the differences in amplitude between this and the entire frequency domain. At  $Re/m=12.5E6$ , the higher amplitudes of the second mode instabilities obtained at  $Z=75mm$  becomes notable in comparison to the other two locations. At even higher Reynolds number, sensor S.5 shows an energy distribution of the disturbances characteristic from a turbulent flow. At the reference position, the boundary layer appears to still be laminar, showing a clear peak corresponding to the second mode instabilities. The higher fluctuation level at the center of the wind tunnel causes higher initial amplitudes of the second mode instability, which then saturates earlier and achieve lower maximum amplitudes than in regions with lower fluctuation levels like  $Z=75mm$ .

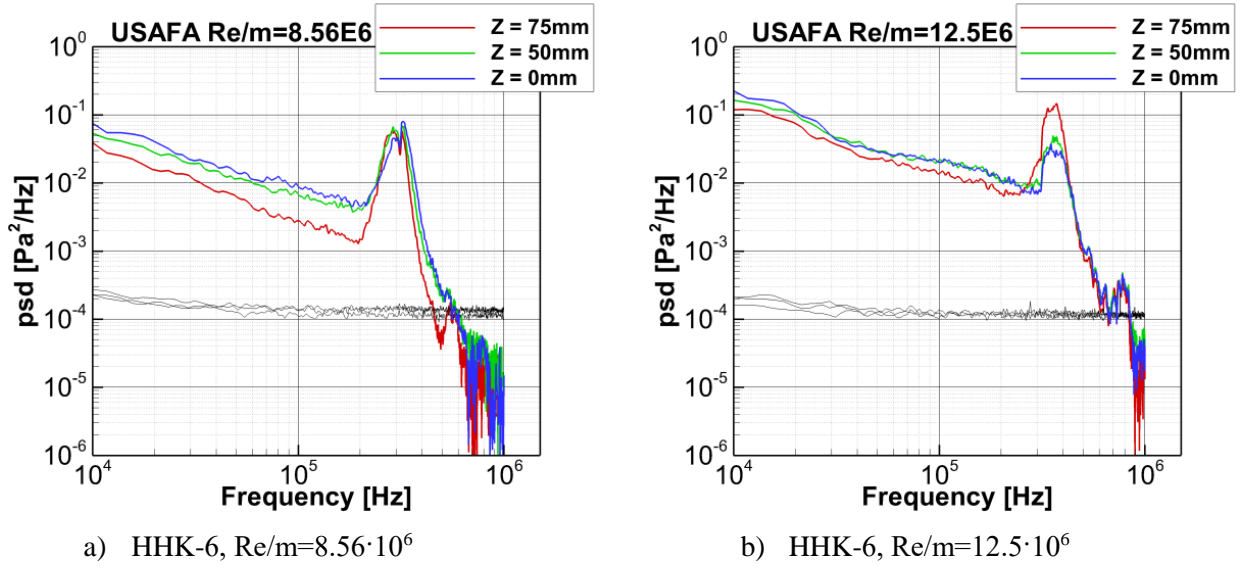


**Figure 29. Noise effect on the second mode instability investigated by changing the vertical position in HHK-6 at different Reynolds numbers**

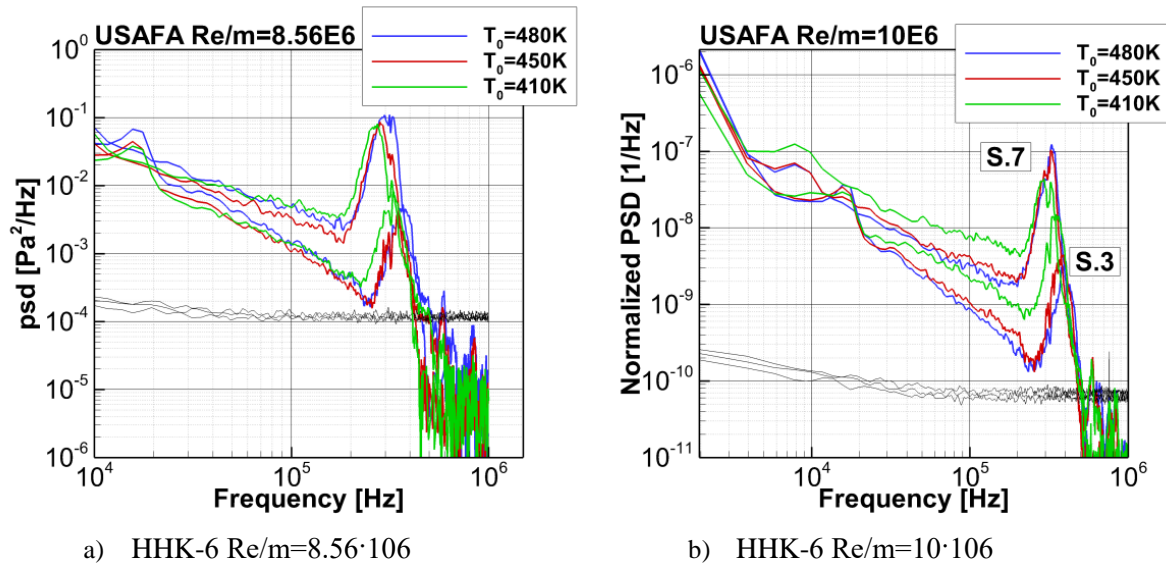


**Figure 30. Temperature effect on the second mode instability investigated by changing the stagnation temperature in HHK-6 at different Reynolds numbers**

In a further test series, the total temperature of the flow was varied in the HHK-6. The effect of the temperature variation on the second mode instability is presented in Figure 30. Each subfigure shows the results of the signals for two sensors (S.3 and S.7) for several Reynolds numbers. When comparing the results for different temperatures, no considerable difference is observed between 450K and 480K. Nevertheless, when the temperature was reduced to 410K, higher levels of pressure fluctuations are obtained at low unit Reynolds numbers combined with lower maximum values of the second mode amplitudes and an earlier saturation. This behavior was also observed when moving the cone towards the center axis of the tunnel where higher fluctuation levels were measured. The transition location shows the same trend. The transition



Reynolds number increased consistently with the stagnation temperature. However, the freestream investigations showed that the noise level increases with the temperature.

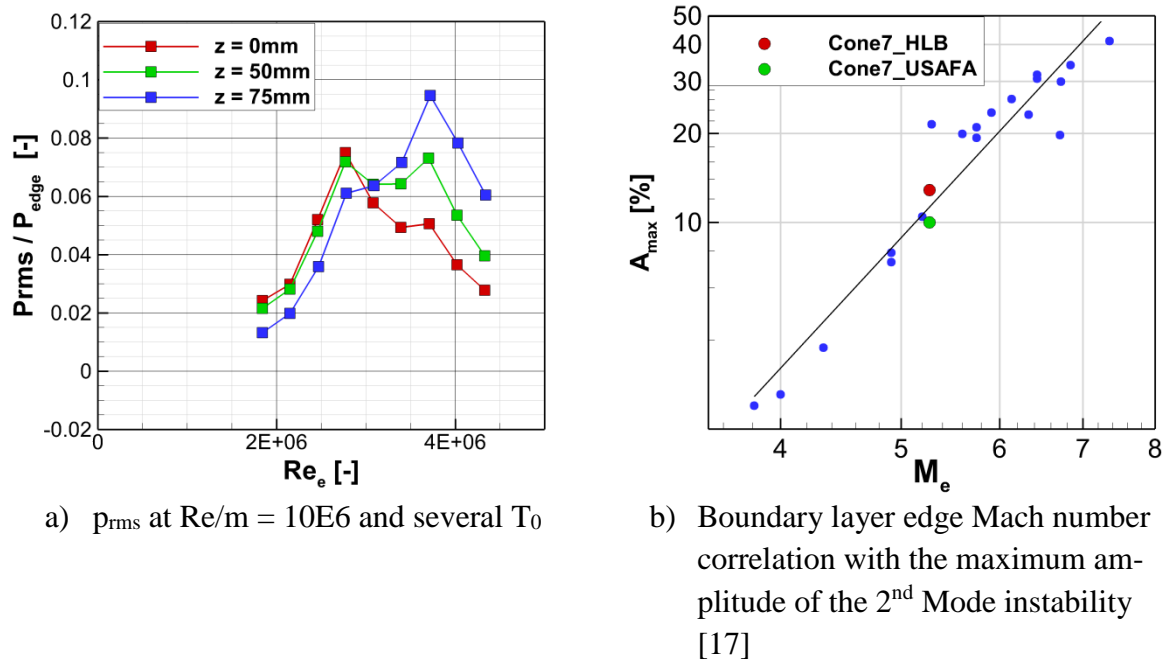


**Figure 31. Prms values of second mode instabilities in HLB and HHK-6**

A comparison of the measured  $p_{rms}$  levels of the second mode instabilities is shown in Figure 31. Before calculating the RMS values of the pressure fluctuations, the signals are filtered around the frequency of the most unstable second mode instability. The pressure fluctuations rise until they reach the point where non-linear interaction takes place and energy is deviated to other frequencies, at which point a decay in the amplitude of the pressure fluctuations is observed. Based on the analysis presented by Marineau, the initial amplitude of the second mode instabilities is proportional to the disturbance level of the incoming flow [17]. Hence, higher levels of pressure fluctuations found in the HHK-6 result in larger initial amplitudes that are visible at low Reynolds numbers. On the other hand, the larger instabilities tend to break down earlier achieving lower maximum amplitudes. Measurements at different temperatures and stagnation pressures show that for all cases the maximum value of the second-modes amplitudes found in HLB was higher than in USAFA.

The maximum value of the pressure fluctuations on a smooth surface in conventional wind tunnels depends only on the Mach number. Marineau showed, by correlating results of several measurements on  $7^\circ$  cones at different Mach numbers and different cone bluntness, that there is a direct correlation between the boundary layer edge Mach number and the maximum pressure fluctuation of the second mode [17]. This relation is shown in Figure 31b. As can be observed, the maximum pressure fluctuations obtained with this model in both wind tunnels agree fairly well with the correlation curve, although sensor S.4 was not properly mounted. The maximum value obtained in the HLB is slightly above the curve and the one obtained in the HHK-6 slightly below the correlation.

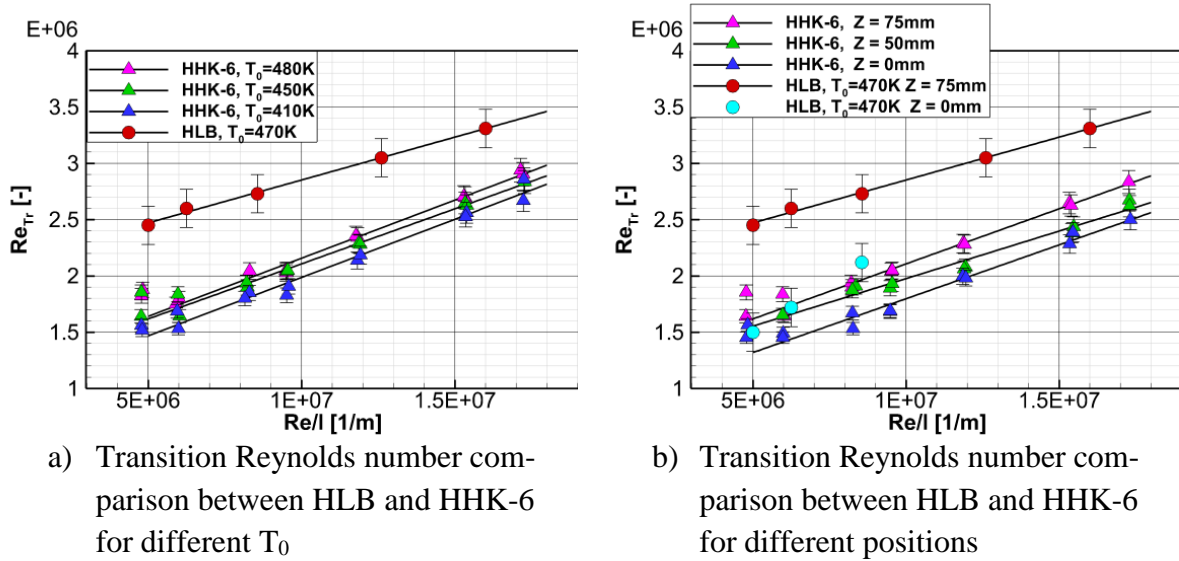


**Figure 32. Transition location analysis based on centerline heat flux from infrared thermography**

The transition location is obtained for several Reynolds numbers by extracting the heat flux at the centerline of the model. Figure 32 presents the transition Reynolds numbers obtained for the same model and similar conditions in both wind tunnels. The transition Reynolds number increases with the unit Reynolds number, and this is a well-known effect in hypersonic flows and has been reported by other researchers in the past [2]. The normalized pressure fluctuations of the free stream decay with the unit Reynolds number, resulting in larger transition Reynolds numbers ( $Re_{tr}$ ) on the surface. The  $Re_{tr}$  found in the HLB are higher than those found in HHL-6. Slightly different dependencies with the free stream Reynolds number was found in both wind tunnels. Note that transition Reynolds numbers obtained on the HLB center line are very similar to the values observed in HHL-6

### 3.3 Capsule Measurements

All of the experiments done within the present work involving the Apollo capsule were conducted at an angle of attack of 24 deg. All measurements were extracted along the center line (symmetry plane) of the model. The transition location on the capsule surface was estimated by analyzing the data obtained from the TEs. The TEs measure the mean temperature of the surface during the run at a high frequency rate. This time series of data is then used to calculate the mean heat flux density, and the transition location is then extracted from these values. The extraction of the exact transition onset is arduous since only discrete values on the surface are obtained. Therefore, additional data from existing numerical simulations is used to rebuild the laminar solution. Then, a polynomial fit is applied combining 12 points from the numerical simulation with three points from the experimental investigations in the transitional region. The transition onset is marked when a deviation higher than 5% is observed between the polynomial curve and the numerical simulation.

The transition experiments were conducted at two locations in both wind tunnels. By moving the capsule away from the center axis, it is exposed to different disturbance levels on the stagnation region. Figure 33a shows the heat flux data obtained with the rough surface ( $k=101 \mu\text{m}$ ) at a  $Re/m = 10E6$  in the HLB. These results show that the transition location remains fairly constant as the capsule is moved to the center axis of the wind tunnel. Thus, the transition is not affected by the higher noise levels measured at the center of the wind tunnel. Therefore, the

transition phenomenon observed with this distributed roughness element can be characterized as roughness induced transition. The distributed roughness generates streamwise vortices, which may interact with initial freestream disturbances, but are rather independent in the developing process. These stationary vortices grow in the vicinity of the stagnation point and disturb the boundary layer causing mode interactions followed by the breakdown of the laminar flow [13].

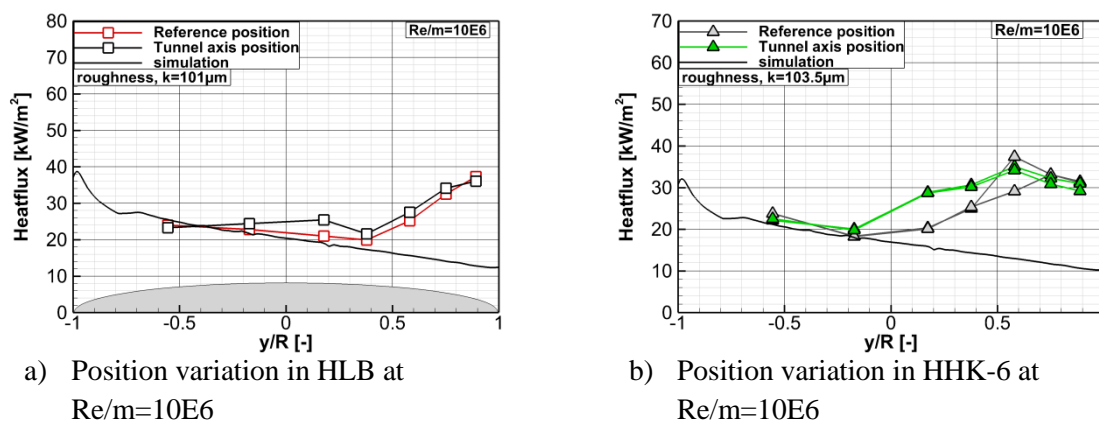


**Figure 33. Heat flux on the capsule surface with variation of  $\text{Re}/m$  and capsule position in both facilities**

Figure 33b, shows the same evaluation conducted in HHK-6. A change in the position of the capsule from the reference position to the center caused a small shift in the transition location. This shift can only be observed at  $\text{Re}/m = 10\text{E}6$ . Measurements at lower and higher Reynolds numbers did not show any influence in the transition location. Nevertheless, when observing the data in detail, an important increment in heat flux values is observed when the capsule was located at the center of the wind tunnel. Measurements conducted in both wind tunnels presented heat flux augmentation at sensor P3. This effect is observed in both wind tunnels for almost all Reynolds numbers investigated. The heat flux augmentation is most likely triggered by the increased levels of vorticity disturbances at the center of the wind tunnel, as described by Marineau [18].

Figure 34a and b show a comparison of the dimensionless heat flux values obtained in the HLB and in the HHK-6 for different Reynolds numbers at the same location in the wind tunnel. The data obtained at  $\text{Re}/m = 8.25\text{E}6$  indicate laminar flow on almost the entire arc length over the surface. The two most downstream sensors showed elevated heat flux values in comparison to the numerical simulations. Although both tunnels presented similar results, higher levels of heat flux were measured close to the stagnation point, sensor P2, in the HLB. This heat flux augmentation effect was also observed by other researchers in different facilities. Conversely, no such phenomenon was observed during the measurements in the HHK-6. Furthermore, the sensor P1 seems to measure a higher heat flux value under this condition, which does not agree with the heat flux obtained from the laminar computations.

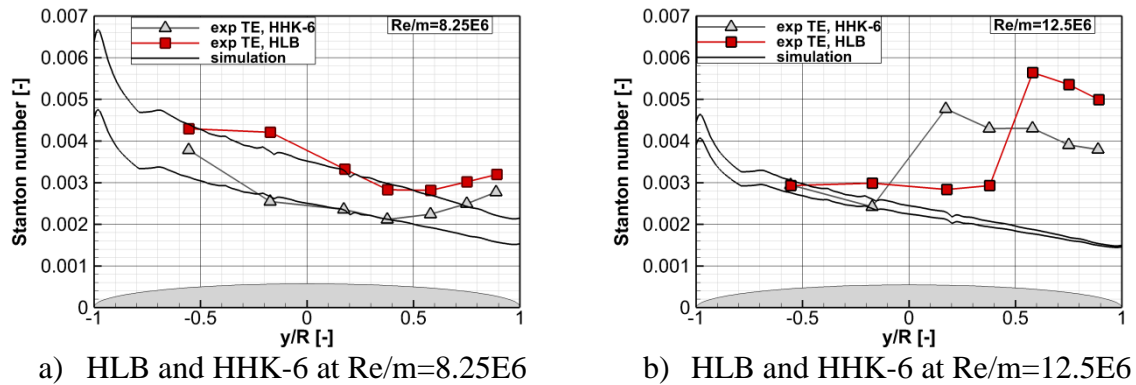


**Figure 34. Heat flux on the capsule surface with variation of  $Re/m$  and capsule position in both facilities**

As the Reynolds number is increased, the transition location moves upstream in both wind tunnels. A difference in the transition location becomes visible above  $Re/m = 10E6$ . The heat flux deviates from the laminar values earlier in HHK-6, and the last three sensors show a decay of the heat flux as expected by a turbulent boundary layer. A substantial difference is observed at  $Re/m = 12.5E6$ , where transition moves further upstream in the HHK-6. In this case, only two of the sensors showed heat flux levels that can be related to laminar flow, while all other sensors presented levels expected in turbulent boundary layers. The earlier transition can be a result of the combination of slightly higher disturbances level of the incoming flow and small height difference of the roughness elements ( $103,5\mu m$  in HHK-6 and  $101\mu m$  in HLB).

The higher temperature range obtainable in HHK-6 allows for measurements at higher temperature than in HLB, which will improve the signal to noise ratio and allow for an investigation on the effect of the temperature on the transition location. A comparison of the differences of the transition location for three different temperatures ( $T_0=470K$ ,  $T_0=511K$ , and  $T_0=615K$ ) is presented in Figure 35. Please note that the measurements at  $T_0=511K$  were conducted at the wind tunnel center axis, and for that reason the capsule was subjected to higher fluctuation levels of the freestream.

The transition location moves upstream in all cases as the Reynolds number is increased. The lowest Reynolds number used in each case for this investigation depends on the blockage created by the model, which prevents the wind tunnel from starting at lower Reynolds numbers. The wind tunnel operates at very low  $Re/m=5.5E6$  while at  $470K$ , but outside the center axis of the tunnel the lowest Reynolds number achievable is  $Re/m=8.25E6$ . For  $615K$  the flow is laminar for the complete streamline along the symmetry plane of the model. This data shows good agreement with numerical simulations.

A direct comparison of the temperature effects for one Reynolds number is presented in Figure 35. The heat flux is presented in the form of the Stanton number, and as a consequence is independent of the free stream temperature unlike raw heat flux. As can be observed, all curves converge making a comparison clearer. This comparison at  $Re/m=8.25E6$  highlights the upstream movement of the transition front. As the temperature is increased, the start of the onset of transition moves closer to the stagnation point. Higher free stream temperatures result in thinner boundary layers making the roughness elements more effective. On the other hand, investigations of the free stream fluctuation levels show a considerable increment as the temperature is increased.

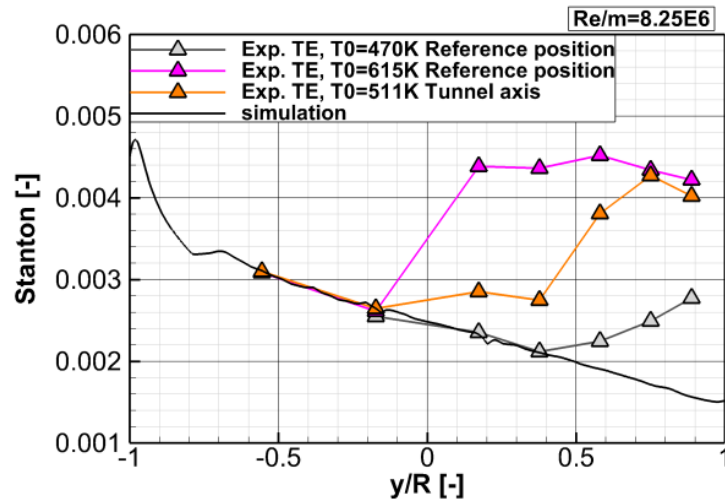
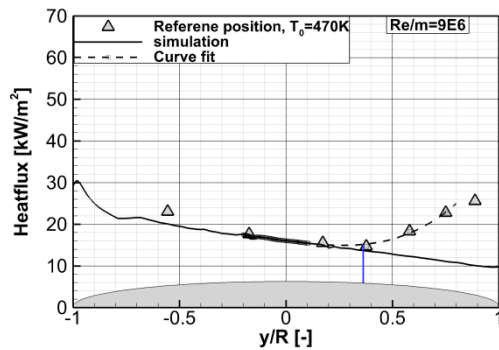
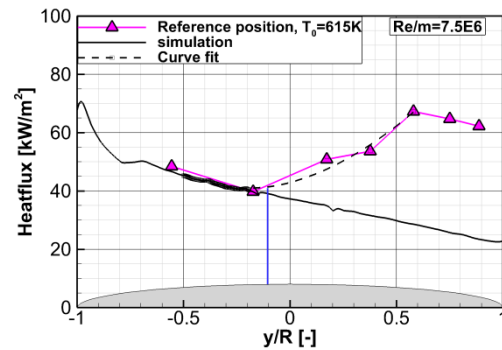


**Figure 35. Normalized heat flux on the capsule surface with variation of  $T_0$  and position in HHK-6 at  $Re/m=8.25E6$**

Figure 36 shows the transition detection method used in the present work for two cases. Figure 36a shows the transition obtained with the capsule at the reference location at  $T_0=470K$  and  $Re/m=9E6$ , and Figure 36b shows the transition location for  $T_0=615K$  and  $Re/m=7.5E6$ . The transition location is detected by combining the points from the numerical simulation with three points in the transition zone. The error related to the estimation of the transition location can, in this way, be reduced. Nevertheless, it is limited to moderate Reynolds numbers for which transition is measured by several sensors.



a) Surface heat flux at  $T_0=470K$ ,  $Re/m=9E6$



b) Surface heat flux at  $T_0=615K$  at  $Re/m=7.5E6$

**Figure 36. Extraction of transition location from heat flux values obtained from the capsule surface at reference position at two conditions showing a) later start of transition onset, b) early transition onset including turbulent flow**

Reshotko and Tumin found a correlation for the observed roughness induced transition on spherical bodies by applying the transient growth theory for stagnation point flows [4]. They investigated the effect of several parameters such as roughness height, wall temperature, and surface curvature. As a result, a model was developed that relates the roughness height, boundary layer momentum thickness and the wall-to-edge temperature ratio to the transition Reynolds number based on the momentum thickness:

$$Re_{\theta, tr} = 180 \left( \frac{k}{\theta} \right)^{-1} \left( \frac{T_e}{2T_w} \right)^{-1.27} \quad (25)$$

The coefficients in this equation were determined carefully by analyzing data of several wind tunnel campaigns. Figure 37 shows the values predicted from the correlation with lines and the comparison with the Reda and PANT experiments conducted in wind tunnels and ballistic ranges. In this figure data from the current and previous tests with the Apollo capsule are included. Two sets of roughness elements measured in the HLB are presented accompanied by a set of data obtained in the HHK-6. The newly obtained data points fall into the expected range and agree well with the correlation model for transient growth. The difference in tunnel noise does not seem to have an important influence on the correlation values. Measurements at higher temperatures bring the values closer to PANT results and correlate well with the  $180(k/\theta)^{-1}$  curve. The higher roughness height results in lower  $Re_\theta$  and higher  $k/\theta$  values, thereby moving points further down the curve.

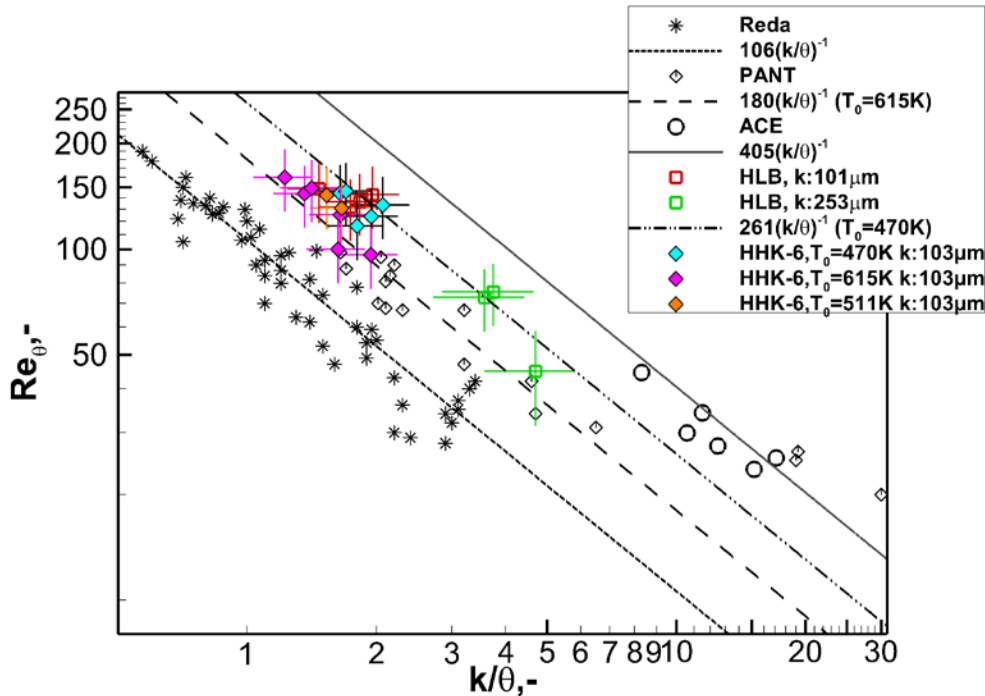


Figure 37. Comparison of transition location on different facilities based on the transient growth theory

## 4 Conclusions

The project objectives were successfully accomplished, and remarkable results on the three proposed research lines were obtained. These are the characterization of freestream disturbances in the Ludwig tubes of TU Braunschweig and Air Force Academy, transition experiments on cones and transition experiments on capsule shapes. The database generated during these experiments serves as starting point for future stability and transition experiments. Comparison of transition on cones in both wind tunnels showed a considerable difference in

the transition Reynolds numbers measured. Additionally, the effect of noise level and the stagnation temperature on the second mode instability was investigated in HHK-6. Higher noise levels generate higher initial amplitudes that cause the second mode to saturate earlier, achieving lower maximum amplitudes. A delay of the transition onset was observed when the stagnation temperature was increased.

Furthermore, a wind tunnel model of the Apollo capsule was used to investigate transition on blunt bodies in both facilities. The transition investigations were conducted using a distributed roughness patch along the surface of the model, and show little dependency of the free stream noise with respect to the transition location. At low Reynolds numbers no important difference in the transition location was observed. At higher Reynolds numbers transition occurred earlier in HHK-6. During the investigation, the stagnation temperature of the flow was varied between 470K and 615K. The results show a significant dependency of the transition location. A considerable upstream shift of the transition onset is observed at higher temperatures.

Transition Reynolds numbers, based on the displacement thickness of the boundary layer and  $k$ -values of the roughness, were computed in order to compare the results with transient growth correlation. Both wind tunnels delivered very similar values for the same free stream temperatures. The obtained data points fall within the expected range and agree well with the correlation model for transient growth.

Freestream measurements were conducted in USAFA and repeated in HLB by means of suited Pitot probes and CTA anemometer. The data obtained from these measurements were analyzed and compared showing higher noise levels at the USAFA wind tunnel. Also measurements with high temperature wire were conducted in HLB. These last showed good agreement with results from DNS simulations of the tunnel nozzle. Different approaches to conduct modal decomposition of the freestream disturbances were scrutinized. It appears that all methods are very sensitive to small variations in the input from CTA data, due to the high conditioning number of the inversion matrixes used to compute fundamental modes from combined probe data. Further methods for measuring freestream fluctuations as well as uncertainty based model decomposition are recommended to avoid unphysical reduction of measured data.

## 5 References

- [1] Mack L.M., "Boundary-layer stability theory," AGARD-R-709, 1984
- [2] Schneider, S. P., "Hypersonic laminar-turbulent transition on circular cones and scramjet forebodies," Progress in Aerospace Sciences, Vol. 40, No. 1, 2001, pp. 1-50
- [3] Pate, S., "Effect on Wind Tunnel Disturbances on Boundary Layer Transition, with Emphasis on Radiated Noise: A Review," AIAA Paper 80-0431, March 1980
- [4] Reshotko, E. and Tumin, A., "Role of Transient Growth in Roughness-Induced Transition," AIAA Journal, Vol. 42, No. 4, 2004
- [5] Theiss, A., Ali, S. R., Hein, S., Heitmann, D., and Radespiel, R., "Numerical and experimental investigation of laminar-turbulent boundary layer transition on a blunt generic re-entry capsule," 44th AIAA Fluid Dynamics Conference, paper No. 2014-2353, 2014
- [6] Schilden, T., and Schröder, W., "Numerical analysis of high speed wind tunnel flow disturbance measurements using stagnation point probes," Journal of Fluid Mechanics, Vol. 833, 2017, pp. 247-273



- [7] Lomas, C. G., "Fundamentals of hotwire anemometry," Cambridge University Press, 2011.
- [8] Smits, A. J., and Dussauge, J. P., "Hot-wire anemometry in supersonic flow," AGARDograph-AG-315, 1989, pp. 5.1-5.14.
- [9] Smits, A. J., Hayakawa, K., and Muck, K. C., "Constant temperature hot-wire anemometer practice in supersonic flows," Experiments in Fluids Vol. 1.2, 1983, pp. 83-92.
- [10] Logan, P., "Modal analysis of hot-wire measurements in supersonic turbulence," 26th Aerospace Sciences Meeting, paper No. 88-0423, 1988.
- [11] Morkovin, M. V., "Fluctuations and hot-wire anemometry in compressible flows," North Atlantic Treaty Organization advisory Group for aeronautical research and development, AGARDograph No. 24, 1956.
- [12] Ali, S. R. C., Radespiel, R., and Theiß, A., "Transition experiment with a Blunt Apollo Shape like capsule in Hypersonic Ludwig Tube., Deutscher Luft-und Raumfahrtkongress, Paper No. 340270, 2014.
- [13] Leidy, A. N., Reshotko, E., Siddiqui, F., and Bowersox, R. D. W., "Transition Due to Roughness on Blunt Capsule: Comparison with Transient Growth Correlation," Journal of Spacecraft and Rockets, Vol. 55, No. 1, 2017, pp. 167-180.
- [14] Batt, R. G., and Legner, H. L., "A Review of Roughness-Induced Nosedip Transition," AIAA Journal, Vol. 21, No. 1, 1983.
- [15] Duan, L., Choudhari, M. M., Chou, A., Munoz, F., Radespiel, R., Schilden, T., Schröder, W., Marineau, E. C., Casper, K. M., Chaudhry, R. S., Candler, G. V., Gray, K. A., and Schneider, S. P., "Characterization of Freestream Disturbances in Conventional Hypersonic Wind Tunnels," , Journal of Spacecraft and Rockets, to appear, 2019.
- [16] Stainback, P. C., and Wagner, R. D., "A comparison of disturbance levels measured in hypersonic tunnels using a hotwire anemometer and a pitot pressure probe," AIAA 7th Aerodynamic Testing Conference, paper No. 72-1003, 1972.
- [17] Marineau, E. C., "Prediction Methodology for 2nd Mode Dominated Boundary Layer Transition in Hypersonic Wind Tunnels," 54th AIAA Aerospace Sciences Meeting, paper No. 2016-0597, 2016
- [18] Marineau, E., Lewis, D., Smith, M., Lafferty, J., White, M., and Amar, A., "Investigation of Hypersonic Laminar Heating Augmentation in the Stagnation Region". 51st AIAA Aerospace Sciences Meeting including the New Horizons Forum and Aerospace Exposition, paper No. 2013-308, 2013.

## 6 List of Publications

### List of and scientific articles published or accepted for publication related to this project or arising from the work:

- [1] Munoz, F., Leinemann, M., Radespiel, R., Semper, M., Cummings, R., Theiss, A., "Transition Measurements on Slender and Blunt Bodies in Ludwig Tubes at Mach



- 6", accepted for publication in AIAA Science and Technology Forum and Exposition January 2019.
- [2] Munoz, F., Radespiel, R., Wu, J., Semper, M., Cummings, R., Schilden, T., Duan, L., "Freestream Disturbances Characterization in Ludwig Tubes at Mach 6," accepted for publication in AIAA Science and Technology Forum and Exposition January 2019.
  - [3] Duan, L., Choudhari, M. M., Chou, A., Munoz, F., Radespiel, R., Schilden, T., Schröder, W., Marineau, E. C., Casper, K. M., Chaudhry, R. S., Candler, G. V., Gray, K. A., and Schneider, S. P., "Characterization of Freestream Disturbances in Conventional Hypersonic Wind Tunnels," , Journal of Spacecraft and Rockets, available online, <https://doi.org/10.2514/1.A34290>, November, 2018
  - [4] Radespiel, R., Ali, S. R., Munoz, F., Bowersox, R. D., Leidy, A., Tanno, H., Kirk, L. C., & Reshotko, E., "Experimental Investigations of Roughness Effects on Transition on Blunt Spherical Capsule Shapes", accepted for publication by Journal of Spacecraft and Rockets, November 2018.
  - [5] E. C. Marineau, E.C., Grossir, G., Wagner, A., Leinemann, M., Radespiel, R., Tanno, H., Wadhams, T.P., Chynoweth, B.C., Schneider, S.P., "Compilation and Analysis of Second Mode Amplitudes on Sharp Cones in Hypersonic Wind Tunnels", accepted for publication by Journal of Spacecraft and Rockets, November 2018.

## 7 List of supported personnel

**Program Officer Name:** Prof. Dr. Russell M Cummings

**Principal Investigator Name:** Prof. Dr.-Ing. R. Radespiel

**Educational Institution:** Technische Universität Braunschweig – Institute of Fluid Mechanics; United States *Air Force Academy, Colorado Springs*

**Name of doctoral Researcher:** Ing. Federico Muñoz

**Name of Research Collaborator:** Dr. Michael Thomas Semper